

RESEARCH

Open Access



# Self-assembly of ZnO-Biochar/Kaolinite/Chitosan/GO with 1D/2D/3D heterojunctions for enhanced removal of estrogens and triclosan in water

Ajibola A. Bayode<sup>1,2,3\*</sup>, Samson. O. Akpotu<sup>4</sup>, Martins O. Omorogie<sup>1,2</sup>, Eny Maria Vieira<sup>3</sup> and Emmanuel I. Unuabonah<sup>1,2</sup>

## Abstract

This Study focuses on the preparation of sustainable and efficient Chitosan catalyst for the removal of three organic pollutants, 17 $\beta$ -Estradiol (E2), 17 $\alpha$ -ethynyl estradiol (EE2) and triclosan (TCS) from water. The prepared nanocomposites were characterized by different techniques which confirmed the presence of the key components Chitosan, *Carica Papaya* seed and Kaolinite. The optical characterization proved the nanocomposite is photoactive with a band gap of 1.81 eV and 1.77 eV for Chitosan/kaolinite biochar (CS/KBC) and Chitosan/kaolinite biochar/GO (CS/KBC/GO) respectively, confirming the ability of the nanocomposite to be active in the visible light region of the spectrum. The degradation experiment using CS/KBC/GO was observed better with 100% removal for 5 mg/L E2 and EE2 over 60 min and 97.8% over 120 min for 10 mg/L TCS at optimum conditions (pH 3 for E2, and EE2 and pH 7). It was observed that the superoxide radical played a major role in the degradation of the contaminants. Furthermore, the CS/KBC/GO was efficient over four cycles without any decrease in performance, which rules out the question of catalyst deactivation proving the sustainability of the catalyst. The toxicity test shows that the water is safe as it does not harm *cerio daphnia silvestrii* organism.; CS/KBC/GO efficiently removed the micropollutants from real-life waste samples and the performance was very good with a slight decrease in performance for the wastewater due to the complex matrix of the water sample that competes for the active site.

**Keywords** Photodegradation, Self assemblage, Toxicity, Water treatment, Emerging contaminants

## Introduction

In recent years, contamination of water resources with toxic micropollutants such as endocrine-disrupting chemicals (EDCs) and personal care products (PCPs) has drawn global attention and this has called for the need for immediate scientific attention to address it [1–3]. Sex hormones such as 17 $\beta$ -Estradiol (E2), and 17 $\alpha$ -ethynyl estradiol (EE2), as well as triclosan (TC) (chemical structures shown in Fig. 1), are frequently found in wastewater and effluent from conventional wastewater treatment plants, surface water and drinking water due to their incomplete removal [4–7].

\*Correspondence:

Ajibola A. Bayode

bayodea@run.edu.ng; ajibolabay7@gmail.com

<sup>1</sup> Department of Chemical Sciences, Faculty of Natural Sciences, Redeemer's University, PMB 230, Ede, Nigeria

<sup>2</sup> African Centre of Excellence for Water and Environmental Research (ACEWATER), Redeemer's University, PMB 230, Ede 232101, Nigeria

<sup>3</sup> Laboratório de Química Analítica Ambiental E Ecotoxicologia (LaQuAAE), Departamento de Química E Física Molecular, Instituto de Química de Sao Carlos, Universidade de Sao Paulo, Sao Carlos, Brazil

<sup>4</sup> Department of Chemistry, Vaal University of Technology, Vanderbijlpark, South Africa



© The Author(s) 2024. **Open Access** This article is licensed under a Creative Commons Attribution-NonCommercial-NoDerivatives 4.0 International License, which permits any non-commercial use, sharing, distribution and reproduction in any medium or format, as long as you give appropriate credit to the original author(s) and the source, provide a link to the Creative Commons licence, and indicate if you modified the licensed material. You do not have permission under this licence to share adapted material derived from this article or parts of it. The images or other third party material in this article are included in the article's Creative Commons licence, unless indicated otherwise in a credit line to the material. If material is not included in the article's Creative Commons licence and your intended use is not permitted by statutory regulation or exceeds the permitted use, you will need to obtain permission directly from the copyright holder. To view a copy of this licence, visit <http://creativecommons.org/licenses/by-nc-nd/4.0/>.

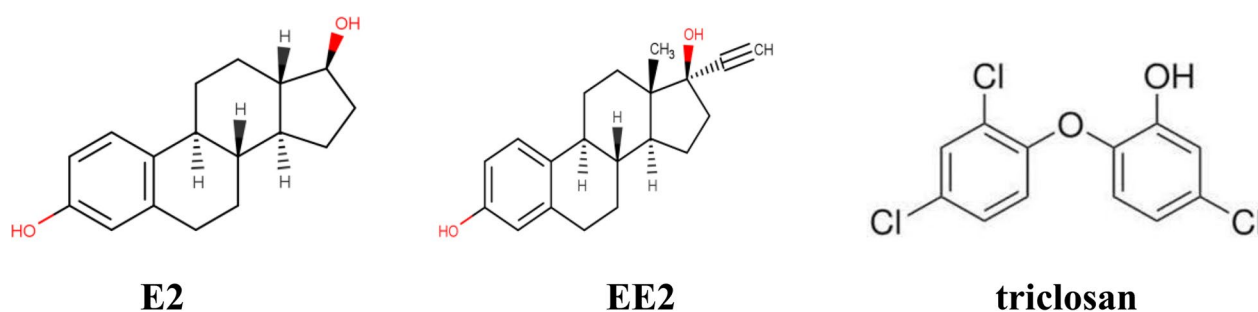


**Fig. 1** The structures of the contaminants E2, EE2 and triclosan

Estradiol is a naturally occurring estrogen present in women and it is the major and most potent form of estrogen while EE2, a derivative of E2, is a synthetic estrogen [8]. Both E2 and EE2 are major components of the contraceptive pill and are also used for hormone replacement therapy. EE2 is more persistent in the environment than E2 because of its complex structure. They are carcinogenic, teratogenic, and mutagenic and they have been linked with the increase in breast-ovarian cancer and fibroids in females, feminization in fishes, obesity, and low sperm count in males, even at low concentrations [8–11].

The world's human population of about 7 billion discharges approximately 30,000 kg/year of natural steroidal estrogen and an additional 700 kg/year of synthetic estrogens solely from the use of birth control pill practices [12]. These estrogens are largely excreted by humans and animals via urine and faeces as active free forms or inactive glucuronide and sulphate conjugates [9, 12].

On the other hand, environmental contamination from chemicals in personal care products (PCPs) has attracted massive attention, due to their negative ecological effects. Triclosan [TCS, 5-chloro-2-(2,4-dichlorophenoxy)phenol] for example, is used extensively in cosmetic and other personal care products like toothpaste, sterilizers, handwash, soap, shampoo as antimicrobial agents [5, 13, 14]. It is toxic to aquatic organisms, bio-accumulative and persistent in the environment [15, 16]. It is considered to be the parent material to other toxic byproducts like dioxins, methyl triclosan and chloroform which may induce hormone disruption, skin irritation, susceptibility to allergy, disruption of the nitrogen cycle in sensitive soils, and antibacterial resistance [16–18]. Approximately 1500 tonnes of TCS are produced annually worldwide, TCS. It has been detected in the environment (natural water bodies) at a level in the range of nanogrammes to microgrammes *per* litre as reported by some researchers [17, 19].

Given these challenges, there is a need for the sequestration of these toxic organic micro-pollutants from

water. There are, however, several techniques that have been developed over the years for the removal of contaminants from water, *e.g.* adsorption [20, 21], membrane separation [22] and advanced oxidation process [23, 24] such as ozonation [25, 26], photolysis [26, 27], photocatalysis, etc. [10, 28]. These methods come with some major shortcomings such as high energy cost, fouling, high cost of operation, high cost of membrane cleansing, disposal of spent adsorbent etc. [29–31]. To be specific the adsorption and photodegradation technologies are receiving far more attention but photocatalysis does top the list because of its capability of completely degrading the contaminant [32].

Photocatalysis is a promising area of research with important applications in various fields. Advancements in catalyst technology have been made, but there are still challenges that need to be addressed [33]. The fast recombination rate of electron–hole pairs and weak photo-stability of catalysts, along with the low surface area of pristine catalysts, limit the efficiency of the catalysts [34]. Researchers have been exploring various strategies to tackle these challenges. Modifying semiconductors, creating heterojunctions [35], and using polymers [36] and carbon supports [2] as stabilizers are some of the approaches that have shown great promise in improving the efficiency and selectivity of photocatalytic reactions. These improvements will have a significant impact on areas such as environmental remediation, energy conversion, and chemical synthesis.

To overcome these major drawbacks, the paper describes the development of a facile chitosan/GO-modified biochar-based photocatalyst for the efficient removal of E2, EE2 and TCS from water. The use of Kaolinite a 1D clay which serves as a support and crushed *Carica papaya* seed serving as a carbon source to reduce the electron–hole recombination of the composite produced stems from their abundance in the environment and conversion of waste to wealth respectively serves as support, Chitosan (CS), a 2D, biopolymer, with amino ( $-NH_2$ ) and hydroxyl ( $-OH$ ) groups which will help prevent

agglomeration and promote stability of the nanocomposite [37, 38].

Graphene oxide is a 2D carbon material, with good mechanical, electrical, thermal and optical properties which has adsorption and photocatalytic ability to remove aromatic compounds with benzene rings through strong  $\pi$ - $\pi$  stacking interaction [39]. Zinc chloride ( $\text{ZnCl}_2$ ) is meant to provide ZnO that enhances the performance of the photocatalytic material in the visible-light region [8].

Different studies have utilized Kaolinite clay [40], Chitosan [38], biochar [41], graphene oxide [42] and their modified form for the removal of organic contaminants in water. In a recent study, Son Tran and his colleagues used biochar/chitosan composite to remove sulfamethoxazole in water [43]. Bacterial Cellulose microfibre-modified chitosan and melamine were synthesized by Mostafi and colleagues for the removal of congo red and it was efficient [44]. Following the upcoming synergistic composition technique, chitosan/metal-based/graphene oxide nanocomposite has not been utilised to remediate contaminants in water. The as-prepared nanocomposites were successfully synthesized and confirmed via different characterization techniques such as FTIR, XRD, SEM, XPS, BET etc. CS/KBC/GO have very good efficiencies for E2, EE2 and TCS degradation. Also, the real-time analysis of treated water samples (tap water and wastewater) to check the degradation efficiency of the synthesized nanocomposite was satisfactory.

### Materials and method

Chitosan ( $\geq 75\%$  (deacetylated), Zinc Chloride  $\text{ZnCl}_2$  ( $\geq 98\%$  anhydrous), sodium chloride  $\text{NaCl}$  ( $\geq 98\%$ ), EE2 ( $> 99\%$ , Sigma), triclosan ( $> 99\%$ ), E2 ( $> 99\%$ ), Alcohol  $\text{CH}_3\text{CH}_2\text{OH}$  (99.7%), methanol  $\text{CH}_3\text{OH}$  (99.9%, HPLC grade), Acetonitrile (99.9%, HPLC grade) (all purchased from Sigma Aldrich, Germany), PTFE filter, graphite flakes, 99% Carbon, -100 mesh ( $\geq 80\%$ ), natural, sulfuric acid  $\text{H}_2\text{SO}_4$  (95% purity), hydrochloric acid  $\text{HCl}$  (37% purity), potassium permanganate  $\text{KMnO}_4$  (99%), hydrogen peroxide  $\text{H}_2\text{O}_2$  (35 wt. % in  $\text{H}_2\text{O}$ ) (all purchased from Lab Synth Brazil), Formic acid ( $\geq 95\%$ ), Acetone (99%) (purchased from Honeywell, Germany), raw Kaolinite clay sourced from Redeem camp, Ogun State, Nigeria and crushed *Carica papaya* seeds sourced from open market, Ede, Osun state Nigeria. The graphene oxide was synthesized using Hummer's method [10].

### Syntheses of nanocomposites

The parent material, made of Kaolinite and *Carica papaya* seeds (KBC) was synthesized according to the protocol in our previous study [8].

### Synthesis of CS/KBC

1 g of chitosan (CS) was dissolved in 50 mL 5% acetic acid at 45 °C for 2 h under constant stirring. Afterwards, The CS solution was added slowly to the 50 mL suspension of 5 g of KBC under stirring for 24 h at 55 °C. The resulting slurry was cooled to room temperature, and CS/KBC was precipitated from the solution using 1 M NaOH solution. The precipitate was filtered and distilled water was used to wash with 0.01 M HCL solution until the pH of the filtrate becomes neutral. The resulting black precipitate, named CS/KBC, was dried at 60 °C and stored in a sample bottle.

### Synthesis of CS/KBC/GO

To synthesize the CS/KBC/GO, a volume equivalent to 10 mg/L of graphene oxide (GO) was added to a suspension of the synthesized CS/KBC composite in Millipore water. The suspension was sonicated for 2 h to ensure homogeneous dispersion. Afterwards, GO-modified CS/KBC composite (CS/KBC/GO) was washed several times with Millipore water and dried at 55 °C for 8 h in a vacuum oven.

### Characterization of the nanocomposite photocatalyst

The Scanning Electron Microscope (SEM) (Leo-Model: 440) equipped with an energy-dispersive X-ray at an accelerating voltage of 5 kV was used to analyze surface morphology and elemental composition. Perkin Elmer spectrum 100 Fourier transform infrared (FTIR) spectrophotometer (USA) was used to analyze the functionalities present in the nanocomposite. The Quantachrome NOVA1000e surface area and particle size analyzer were used to determine the Brunauer-Emmett-Teller analysis. X-ray photoelectron spectroscopy (XPS) was conducted using a Thermo Scientific K-Alpha spectrometer with a monochromatic Al  $\text{K}\alpha$  (1486.6 eV) radiation source.

### Photocatalytic performance of CS/KBC and CS/KBC/GO

The degradation of E2, EE2 and TCS in 100 mL aqueous solution of 5 mg/L E2 and EE2 and 10 mg/L TCS was examined under visible light (room temperature = 25 °C, four fluorescent lamps = 35 W each, distance of lamp from reacting vessel = ca 4 m) with the photocatalytic activity of the prepared materials CS/KC and CS/KBC/GO. The process was carried out by agitating 0.2 g of the catalyst (CS/KBC, CS/KBC/GO) on a shaker for 400 and 600 min for E2, EE2 and TCS respectively. At specific time intervals, samples were withdrawn and filtered through 0.25  $\mu\text{m}$  PTFE syringe filters, and the analysis was carried out in triplicate. The remnant contaminants (E2, EE2 and TCS) were quantified using high-performance liquid chromatography (HPLC, Agilent 1200

series HPLC–DAD detector at a wavelength of 285 nm for E2 and 280 nm for TCS). Gradient elution was performed with a flow rate of 1 mL/min, and an injection volume of 20  $\mu$ L for 12 min using a mixture of acetonitrile and water spiked with 0.1% formic acid (3 min: 30/70%; 4 min: 40/60%; 10 min: 45/65%; 13 min: 30/70%) for the E2 and EE2. For TCS, isocratic elution was employed using a mixture of acetonitrile and water spiked with 0.1% formic acid. Separation was achieved using a Zorbax SB-CN (5  $\mu$ m) reverse phase (4.6  $\times$  250 mm) column.

#### Effect of operational variables

The degradation process was investigated using the CS/KBC/GO photocatalyst with the highest efficiency by examining the initial concentration of organic contaminants, photocatalyst dosage, ionic strength, anions, and pH. The effect of photocatalyst dosage was analyzed by mixing 0.02, 0.04, 0.06, 0.1, 0.2, 0.3, and 0.4 g/L of the photocatalyst with 5 mg/L (E2 and EE2) and 10 mg/L (TCS). To examine the impact of pH on photocatalyst efficiency, the pH of each solution containing E2, EE2, TCS, and 0.2 g of photocatalyst was adjusted between 2.0 and 12.0.

#### Scavenging experiment

Different radical scavengers like benzoquinone (BQ), isopropyl alcohol (IPA), and ammonium oxalate (AO) were utilized to investigate the reactive species produced by the CS/KBC/GO material with the best photocatalytic efficiency in this study. The scavengers were used to trap HO $\cdot$ ,  $\cdot$ O $_2^-$  and h $^+$  respectively in aqueous systems. In addition, 0.05 mM of the different radical scavengers were added to spike the 5 mg/L E2 and EE2 and 10 mg/L TCS.

#### Competitive degradation of micropollutants

To examine the impact of a combination of E2, EE2, and TCS micropollutants on the effectiveness of CS/KBC/GO, a study was carried out. The study included 0.2 g/L of photocatalyst, 5 mg/L of E2 and EE2 and 10 mg/L of TCS. The samples were collected after 480 min for E2 and EE2 and 600 min for TCS. Each sample was filtered through a 0.25- $\mu$ m filter and analyzed using the HPLC–UV. The samples were analyzed three times to ensure accuracy.

The amount of the micropollutant degraded was calculated using.

$$\% \text{ Degradation} = \frac{C_o - C_e}{C_o} \times 100 \quad (1)$$

$C_o$  represents the initial concentration in mg/L.  $C_e$ , on the other hand, refers to the equilibrium concentration of in mg/L. To determine the degree of mineralization in

water treated with photocatalysts, the oxygen equivalent of organic matter in each sample was measured using the Shimadzu TOC VCPH Analyzer (P/N 638–91062-33; S/N 39N42773).

#### Treatment of real-life sample

A study was conducted on the efficacy of the CS/KBC/GO composite, which is the most effective photocatalytic material, in breaking down steroid estrogens (E2, EE2, and TCS) in tap water, rainwater, and wastewater obtained from the wastewater sewer at the University of Sao Paulo, Sao Carlos, Brazil (22.0027 $^\circ$  S, 47.8986 $^\circ$  W). These matrices were spiked with 5 mg/L E2 and EE2, and 10 mg/L TCS.

## Results and discussion

#### Characterizations of the nanocomposites

The XRD was used to confirm the level of crystallinity of the materials, chitosan, Kaolinite, CS/KBC, and CS/KBC/GO as shown in Fig. 2A. The presence of the broad peak at  $2\theta = 10.01$  (020), 20.04 (110) which confirms the semi-crystalline nature of the chitosan [45, 46]. Kaolinite characteristic 001 reflections are observed at 12.4 $^\circ$  (JCPDS 79–1570) in all kaolinite, CS/KBC and CS/KBC/GO. Other Kaolinite reflections were all observed at  $2\theta = 20.9$  (020), 23.5 (110), 45.7, 54.9 and 60.0 $^\circ$  (ICSD 66571). Quartz peaks were also observed in all the photocatalysts at  $2\theta = 21.6$  (020), 26.8 (111), 36.7(200), 38.2(131) and 50.3 (033) (ICSD 46–1045), as confirmed in our previous studies [10, 35]. Carbon peaks were detected in the synthesized CS/KBC and CS/KBC/GO XRD pattern at 42.47 $^\circ$  (100) due to BC used in synthesizing the composite.

CS/KBC and CS/KBC/GO composite were all characterized by the presence of ZnO phase at  $2\theta = 31.6$  (100), 36.6 (101), 46.0 (102), 62.5 $^\circ$  (103) which resulted from the use of ZnCl $_2$  and NaOH hydroxide for the preparation of the parent material KBC. The wurtzite phase of zinc was also reflected at 34.3 (002), 36.6 (101) and 46.1 $^\circ$  (102) for both catalysts [46]. CS/KBC/GO was characterized by the typical GO reflection at  $2\theta = 10.0^\circ$  [8]. The successful confirmation of the wurtzite phase and the GO in the as-synthesized composite aided their photocatalytic performance compared to the parent material KBC.

FTIR analysis of the photocatalyst was obtained between 4000 and 400  $\text{cm}^{-1}$  for all photocatalysts (Fig. 2B). The absorption peaks between 3720 and 3400  $\text{cm}^{-1}$  are attributed to -OH and -NH groups stretching vibrations [47]. However, for the samples, KBC, CS/KBC, and CS/KBC/GO, the stretching -OH vibration groups lie between the tetrahedral and octahedral sheets of the clay (Kaolin). Furthermore, the -OH stretching group from the octahedral surface forms hydrogen bonds

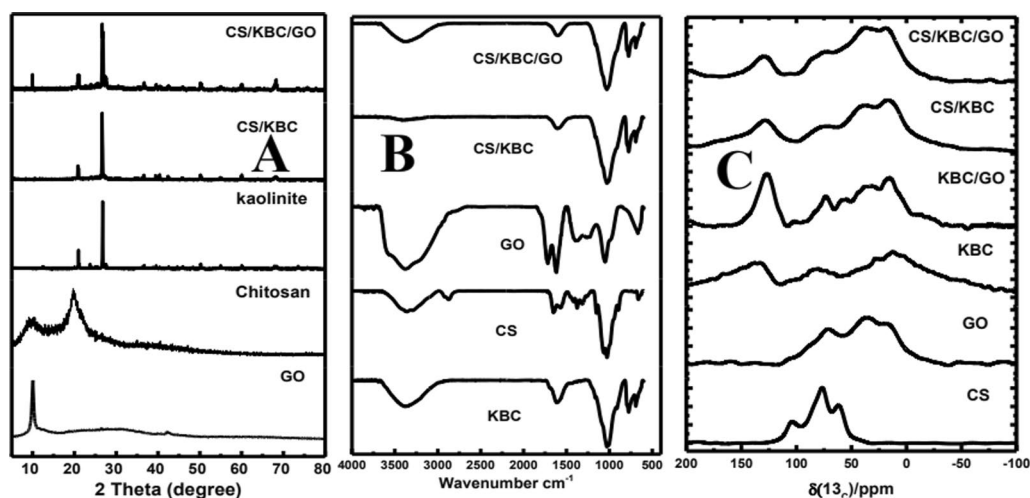


**Fig. 2** A X-ray diffraction pattern, B Attenuated total reflectance-FTIR (C)  $^{13}\text{C}$  NMR of Chitosan, Kaolinite, GO, CS/KBC and CS/KBC/GO nanocomposite photocatalyst

with the oxygen of Si–O–Si bonds on the lower surface of the upper layer [48]. This observation conforms to the study by Akpotu and his colleagues [49]. The absorption band at around 1636 and 1626  $\text{cm}^{-1}$  is assigned -OH and -NH bending vibrations. The absorption band at around 994–1010  $\text{cm}^{-1}$  is assigned as horizontal Si–O bending vibration. The peak between 805 and 782  $\text{cm}^{-1}$  was assigned as Si–O–Si inter-tetrahedral bridging bonds in  $\text{SiO}_2$  and -OH deformation bands of gibbsite. GO has a high amount of oxygen functional groups after oxidation with strong acids. The peak around 1715  $\text{cm}^{-1}$  can be attributed to C=O stretching ketone and aldehyde groups. The peak around 1170  $\text{cm}^{-1}$  was assigned as the C–O stretching carboxylic group. The peak around 1030  $\text{cm}^{-1}$  was assigned as C–O stretching alcohol and phenol groups [47, 50]. For chitosan (CS), the absorption bands around 1650 and 1595  $\text{cm}^{-1}$  are attributed to  $\text{CONH}_2$  and  $\text{NH}_2$  groups, respectively. However, these peaks were hypsochromically shifted but appeared with lower intensity in CS/KBC and CS/KBC/GO. This phenomenon can be attributed to the interaction of the  $\text{NH}_3^+$  group of the chitosan with the hydroxyl, carbonyl and carboxyl groups of the Kaolinite and the Kaolinite biochar [51, 52]. The absorption band which appeared around 1000  $\text{cm}^{-1}$  in CS/KBC and CS/KBC/GO is due to Si–O–C vibration [53]. The shift and presence of a new peak indicates the interaction between the GO, chitosan, biomass, and Kaolinite. The peak at 572–456  $\text{cm}^{-1}$  suggests the presence of a Zn–O stretching band and oxygen vacancies in ZnO [8] which confirms the result of the XRD.

The  $^{13}\text{C}$  NMR spectra of the photocatalyst were different in functional groups (Fig. 2C). The NMR spectra for

the GO, KBC/GO (Kaolinite mixed with GO and *Carica papaya* seed) and CS/KBC/GO. The chitosan (CS) spectra show peaks at around 180 and 105 ppm which corresponds to carbonyl and anomeric carbons, respectively. The peaks around 60 ppm correspond to the C6/C2 pyranose ring from cellulose. The peak around 75 ppm is assigned to the C3/C5 resonances [54, 55]. For GO, the peak around 60 ppm denotes the epoxide groups (C–O–C) and the peak around 70 ppm denotes the carbon adjacent to hydroxyl groups (C–OH) [56]. The peak around 100 ppm is lactol and carbonyl groups, while the peak around 160 and 190 ppm was designated as O=C–O and ketone carbonyl groups [57]. KBC/GO and CS/KBC/GO spectrum exhibit peaks which are typical of lignocellulosic biomass composed of lignin and cellulose. The peak around 56/57 ppm is assigned to lignin methoxy groups [58]. The peaks around 90–60 ppm are assigned as carbonilic carbons. The peaks around 66 and 62 ppm are assigned as aliphatic C6 from cellulose. The peaks around 73 and 75 ppm are assigned as C2 and C5, respectively. Peaks present around 89–84 ppm are assigned as the crystalline and surface chain of cellulose present in the biochar and C1 is found in the 91–83 ppm range [59]. In KBC/GO and CS/KBC/GO, the peaks around 157–110 ppm can be assigned as lignin [60]. In CS/KBC/GO, the peak around 170–187 ppm can be assigned as carboxylic carbons from the acetyl group [61].

The X-ray photoelectron spectroscopy (XPS) analysis was carried out to confirm the chemical composition and elemental valence state of the CS/KBC/GO nanocomposite photocatalyst [62]. The XPS spectrum in Fig. 3A shows the scan of the photocatalyst and it confirmed the presence of C, N, O and Zn which agrees with the EDX.

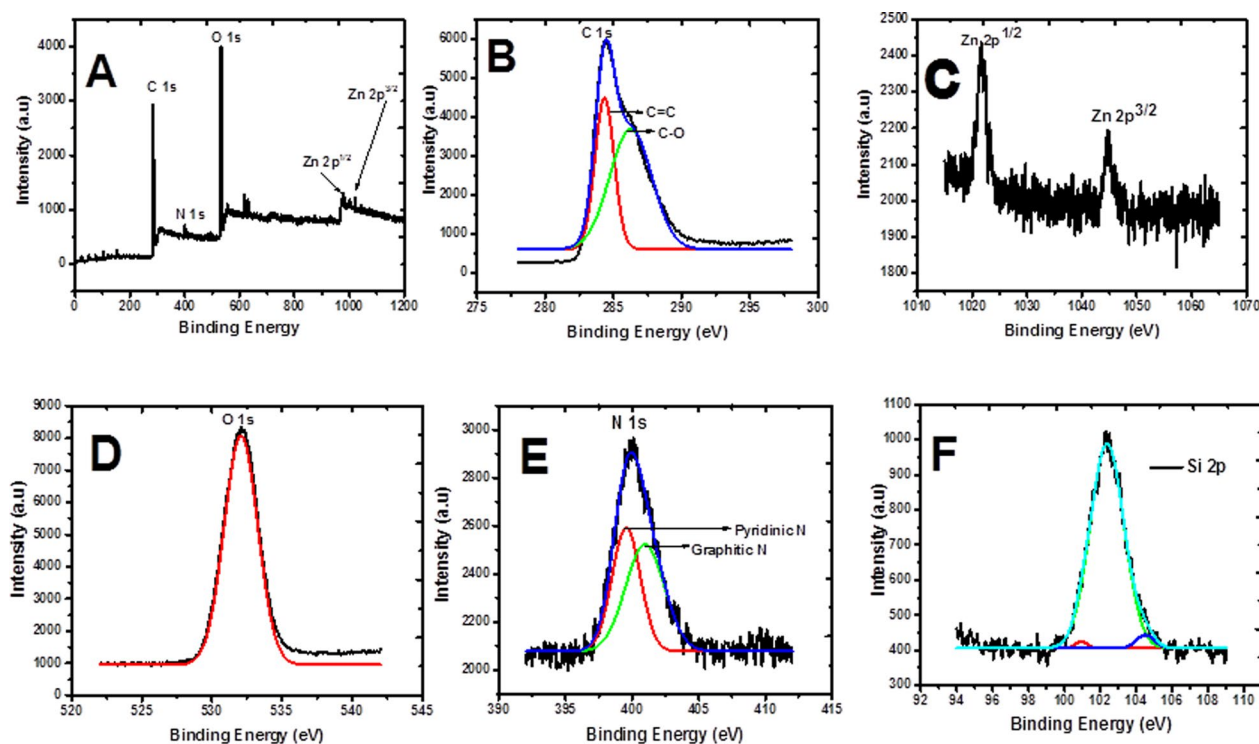


**Fig. 3** X-ray Photoelectron Spectroscopy (XPS) (A) scan (B) C 1 s spectrum (C) Zn 2p (D) O 1 s spectrum (E) N 1 s spectrum (F) Si 2p spectrum of CS/KC/GO nanocomposite photocatalyst

Figure 3B XPS spectrum confirms the presence of C with an asymmetric peak at 284.6 eV (Fig. 3B). The deconvoluted peaks at 284.2 and 286.2 eV confirm the presence of C=C and C-O respectively. The Zn 2p<sup>1/2</sup> and Zn 2p<sup>3/2</sup> chemical states of Zn are seen at 1022 and 1044.7 eV respectively (Fig. 3C). The peak at 531.6 eV as shown in Fig. 3D, confirms the presence of oxygen species.

The peak at 399.96 suggests N is available in the system. The two de-convoluted peaks that appeared after the deconvolution of the N1s spectra at 399.96, 399.52 and 400.96 eV (Fig. 3E) are associated with sp<sup>2</sup> hybridized N atoms in tertiary nitrogen and terminal amino function (-C-N-H) [63]. The peak at 102.0 eV suggests the Si 2p chemical state which confirms the presence of kaolinite clay in the composite make-up (Fig. 3F).

Brunauer–Emmett–Teller technique was used to characterize the photocatalyst CS/KBC and CS/KBC/GO. The two photocatalyst composites show a type IV adsorption–desorption isotherm according to the IUPAC classification. It also shows the H3 hysteresis loop signifying slit-like formed pores with non-uniform particle size [32] (Fig. 4A, B). This indicates that the photocatalyst is mesoporous. The surface area of the CS/KBC and CS/KBC/GO photocatalyst are 128 and 168 m<sup>2</sup>/g respectively as shown in Table 1. After adding GO, an enhancement in surface area was noticed, possibly because of

the high intrinsic surface area of GO resulting from its 2D sheet-like structure. When interacting with CS/KBC, GO increases the surface area further due to its large, flat, and thin layers. Each separate GO sheet can substantially contribute to the composite's overall surface area by exposing more reactive sites.

The scanning electron microscopy (SEM) images of the prepared photocatalytic composite CS/KBC show irregularly shaped small particles with agglomerations (Fig. 5A). The image of the CS/KBC/GO showed largely aggregated particles in lumps and the typical flaky morphology of the GO because of the modification with GO. These results suggest that the prepared photocatalysts are composites (Fig. 5B). The EDX of the photocatalyst as shown in Fig. 5C and D confirm the presence of Ti, O, Fe, Zn, Al, P, Si, S, and Ca in them. The Zn and Cl are a result of the ZnCl<sub>2</sub> used for activating the parent material KBC, the Si, Ti, Fe, and Al stem from the Kaolinite clay, while K and Fe are major components of *Carica papaya* seed [64]. The EDX result did not reveal the presence of carbon. Still, the XPS did because it is more accurate for surface analysis. It provides detailed information on the chemical state and precise quantification of elements at the surface with high energy resolution.

Figure 6A shows the optical absorption spectrum of CS/KBC and CS/KBC/GO photocatalytic composite

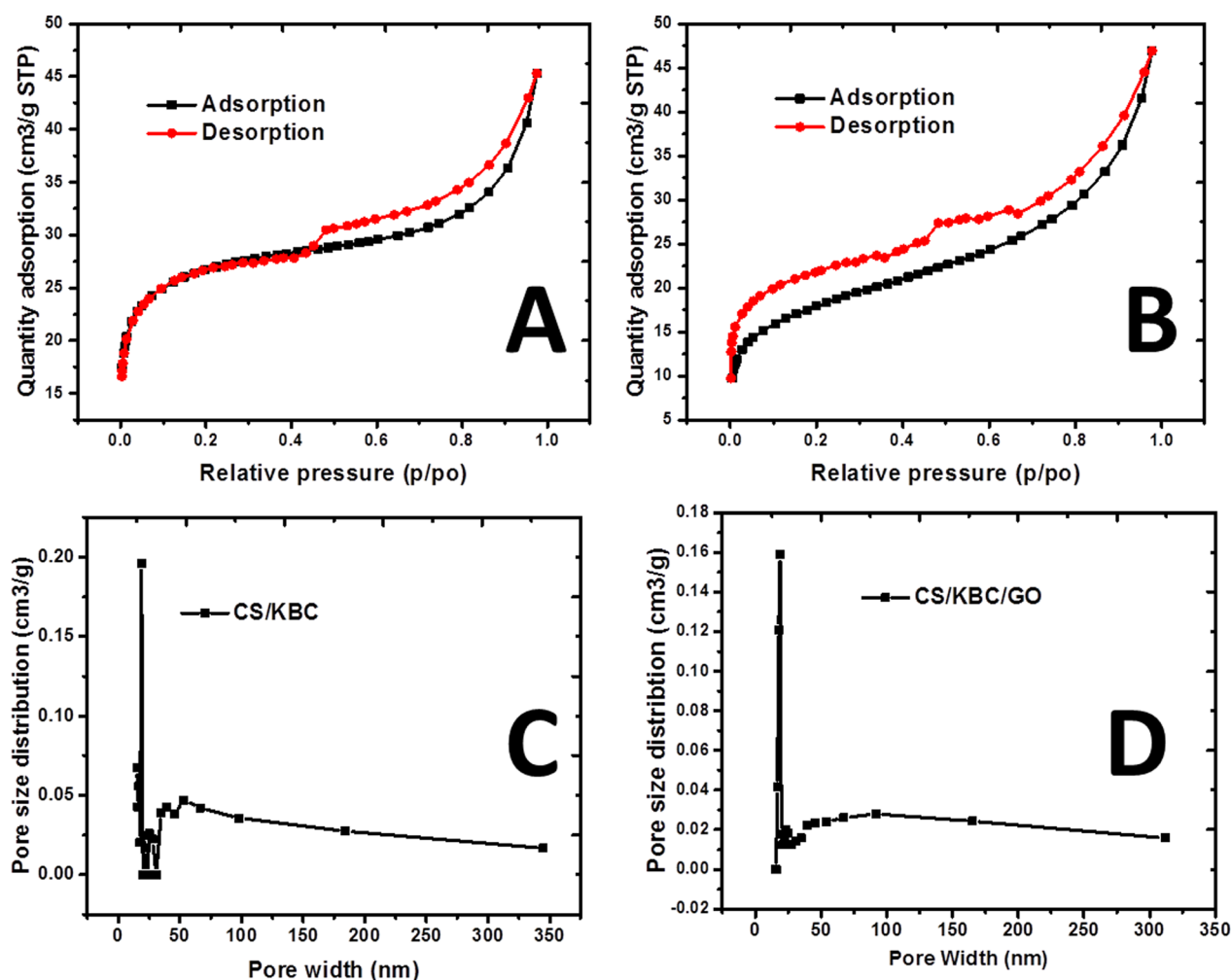


**Fig. 4** N<sub>2</sub> adsorption/desorption isotherm (A) CS/KBC, (B) CS/KBC/GO, and Pore size distribution plot (C) CS/KBC, (D) CS/KBC/GO photocatalyst composite

**Table 1** Brunauer–Emmett–Teller (BET) surface area, pore volume and pore size of the as-synthesized photocatalytic composite

Composite	Surface area (m <sup>2</sup> /g)	Pore volume (cm <sup>3</sup> /g)	Pore size (Å)
CS/KBC	128	0.098	16.42
CS/KBC/GO	168	0.072	20.4

recorded at wavelengths between 200 and 800 nm using UV-DRS equipment. The CS/KBC shows absorption edge at 260 nm and 489 nm and CS/KBC/GO at 220 nm, 287 nm and 487 nm. The estimated bandgap obtained from Tauc analysis using the indirect  $n$  values are estimated to be 1.81 and 1.77 eV for CS/KBC and CS/KBC/GO nanocomposites, respectively (Fig. 6B).

The UV and visible light absorption edges of CS/KBC and CS/KBC/GO photocatalysts suggest these

nanocomposites can trap and utilize light from solar light with a spectrum ranging from ultraviolet to infrared. The catalyst becomes more active in the visible region, resulting in the generation of additional electron–hole pairs. This, in turn, leads to the excited electrons in the conduction band reducing oxygen to superoxide anion. In contrast, the hole in the valence band is a strong oxidizing agent that can react with water and hydroxide ions to form hydroxyl radicals' reactive oxygen species (ROS). These species are essential for facilitating oxidation–reduction reactions in photocatalysis, making the process more efficient for various applications such as environmental remediation, energy conversion, and pollutant breakdown [10, 62].

#### Photocatalytic activity and mineralization experiment

A comparison study between all the components of the photocatalyst Chitosan, Kaolinite, CS/GO, KBC, CS/

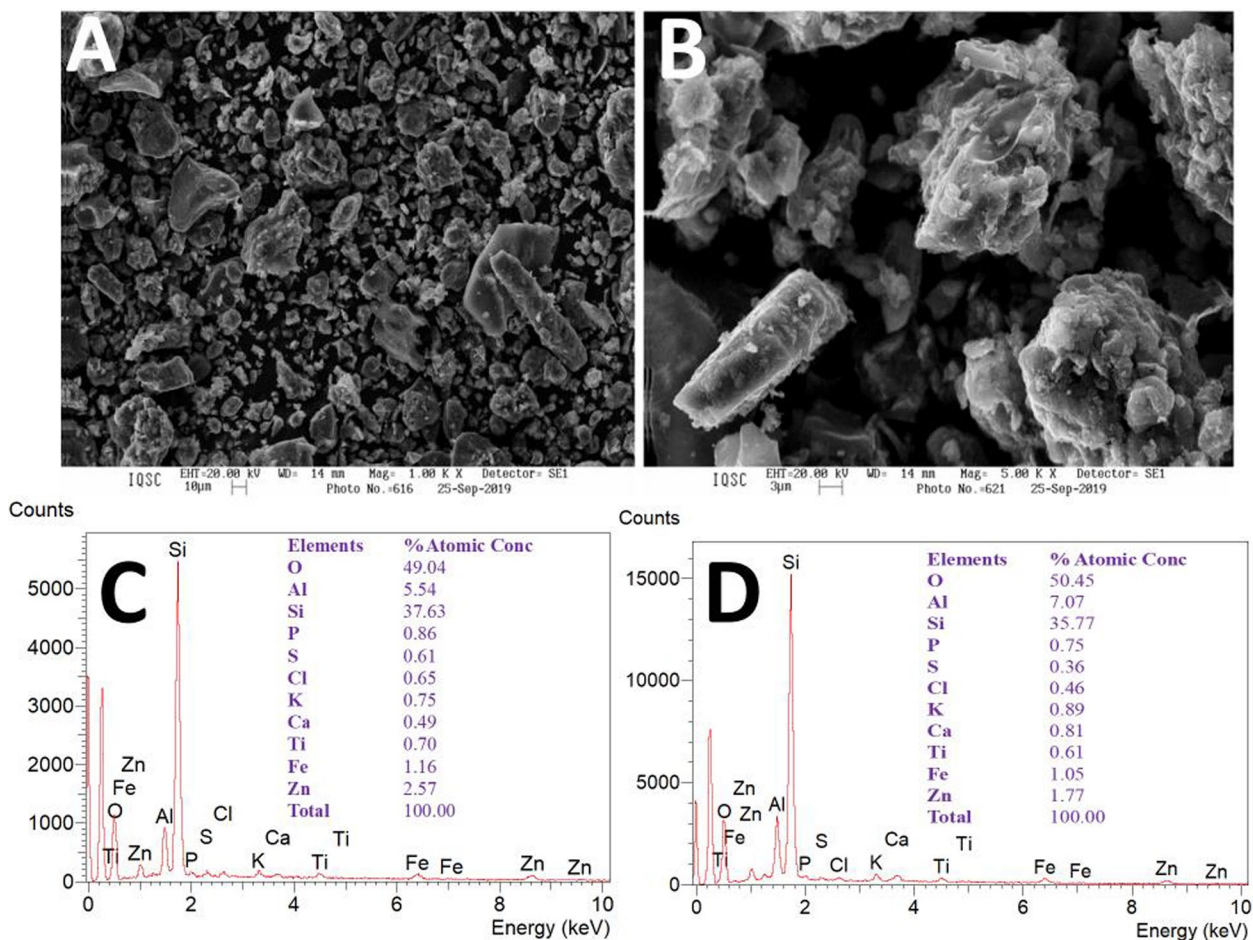


**Fig. 5** **A** Scanning Electron Microscope images of CS/KBC, **B** CS/KBC/GO photocatalytic composite **C** Energy Dispersive X-ray of CS/KBC and **D** CS/KBC/GO photocatalytic composite

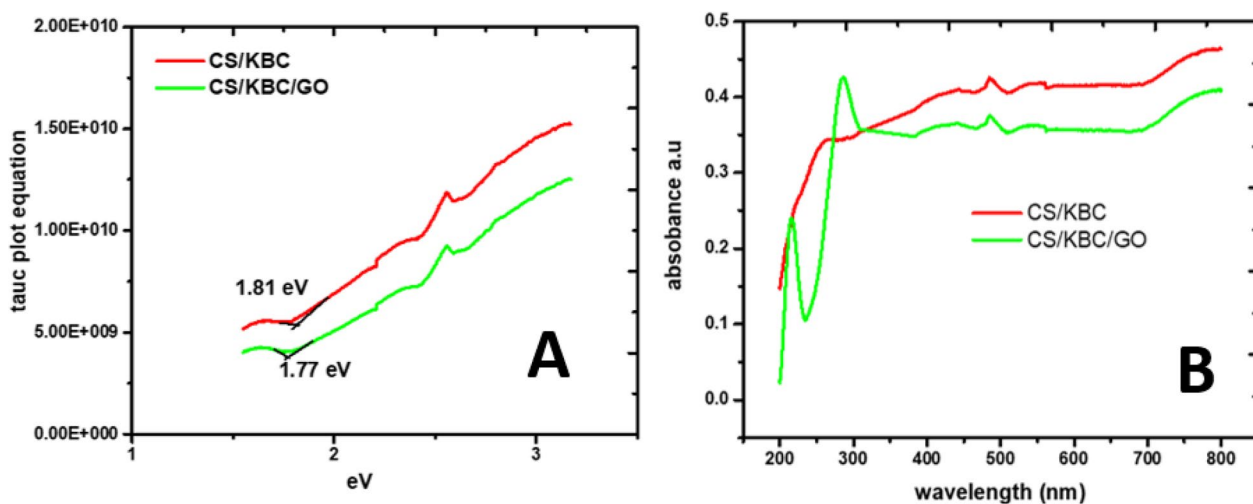


**Fig. 6** **A** UV-DRS and **B** Tauc plot of CS/KBC and CS/KBC/GO photocatalytic composite

KBC, and CS/KBC/GO was conducted in a preliminary evaluation to determine their capacity to degrade the contaminants. The preliminary evaluation revealed the performance of Chitosan, Kaolinite, and CS/GO, KBC showed that the removal of the contaminant was less than 25%, while CS/KBC and CS/KBC/GO showed good performance of over 60% and 90% respectively (Fig. 7A).

To examine the photocatalytic activity of the materials, a photolysis experiment (in the presence of visible light with no nanocomposite) was carried out for the degradation of E2, EE2 and TCS with an observed removal efficiency of 19.62%, 14.24% and 8.967% respectively (Fig. 7B). In the absence of light irradiation, the nanocomposite CS/KBC showed removal efficiencies of 9.34%, 7.90%, and 5.34% for E2, EE2, and TCS, respectively. On the other hand, the removal efficiencies using CS/KBC/

GO were 19.20%, 11.94%, and 15.71% for E2, EE2, and TCS (Fig. 7C).

The photocatalytic experiment was performed using both binary CS/KBC, ternary CS/KBC/GO nanocomposites and CS/KBC showed degradation efficiency of 64.6%, 68.12% and 67.85%, while CS/KBC/GO showed degradation efficiency of 100%, 100% and 97.8% for E2, EE2 and TCS respectively. The results proved that the ternary nanocomposite CS/KBC/GO have better efficiencies than the binary CS/KBC. It showed 100% for E2 and EE2 in <60 min and 97.87% for TCS in <120 min as observed in Fig. 7B, C below. This proves that the irradiation of visible light enhanced the removal of the contaminant over a short period. Also, the enhanced performance of the ternary CS/KBC/GO nanocomposite can be attributed to the presence of the GO which reduces the bandgap and makes it more available to absorb light in the visible

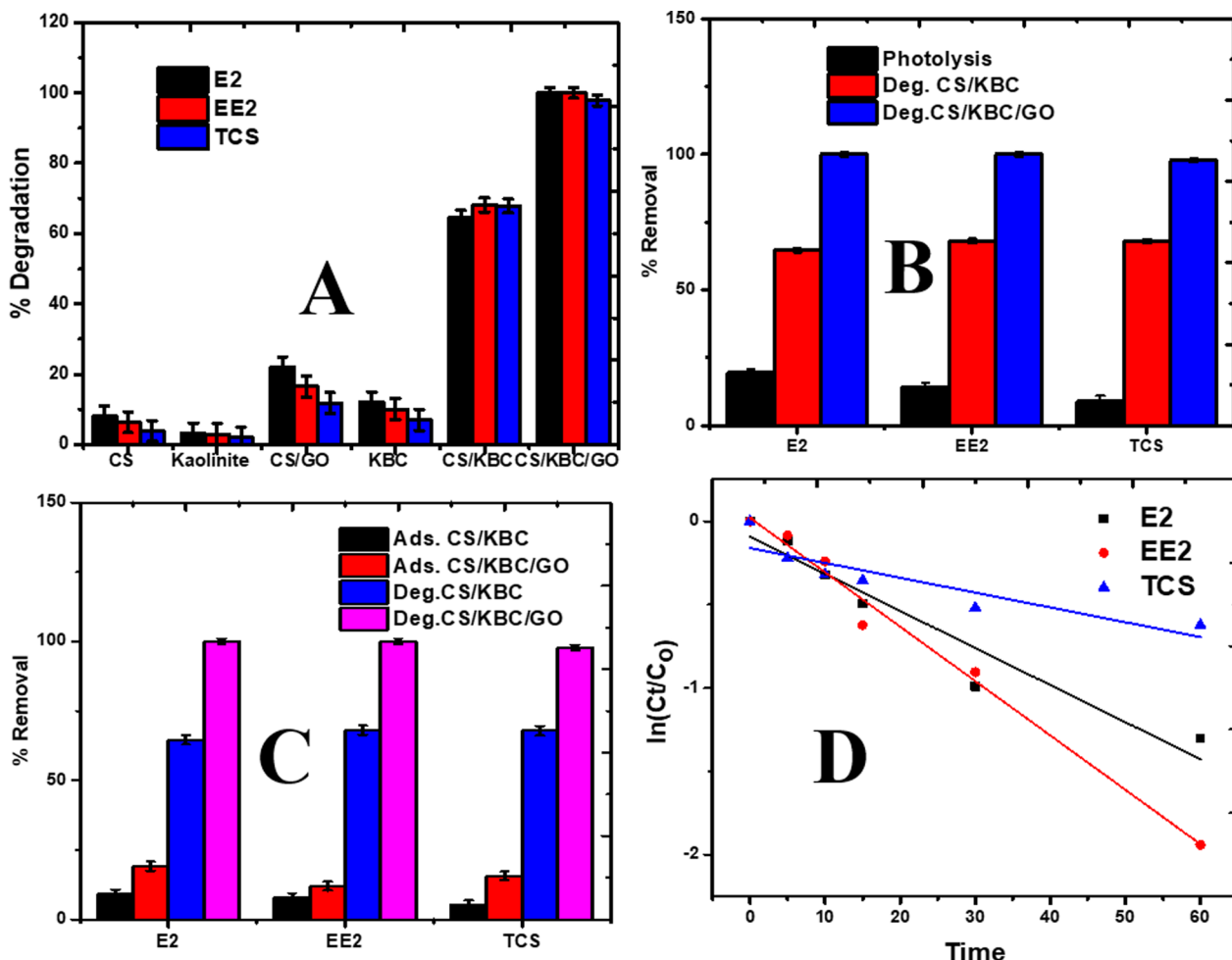


**Fig. 7** A The different components of the photocatalyst performance for degradation, B Photolysis and photodegradation of E2, EE2 and TCS using CS/KBC and CS/KBC/GO, (C). Photodegradation and adsorption process for the removal of E1, E2 and TCS using CS/KBC/GO and (D). kinetic Model for the degradation of E1, E2 and TCS using CS/KBC/GO. (Conditions: 100 mL of 5 mg/LE2 and EE2, 100 mL of 10 mg/L TCS, 0.2 g CS/KBC and CS/KBC/GO, temperature 25 °C, pH 3 for E2 and EE2 and pH 6 for TCS)

region, also, it reduces the recombination rate of the electron–hole pair generated, which in turn increases the formation of hydroxyl ( $\cdot\text{OH}$ ) and super-oxide radicals ( $\cdot\text{O}_2$ ) aiding the optimum degradation of E2, EE2 and TCS [32, 33, 65].

Figure 7D shows that the photodegradation of E2, EE2 and TCS by CS/KBC/GO fit the pseudo-first-order kinetic equation, which is:

$$\ln \frac{C_t}{C_o} = -k_{app}t \quad (2)$$

where  $k_1$ , is the rate constant ( $\text{min}^{-1}$ ),

$C_o$ , is the equilibrium concentration of E2, EE2 and TCS ( $\text{mg. L}^{-1}$ ),

$C_t$ , is the concentration of E2, EE2 and TCS at time  $t$  (min), respectively.

The rates of photocatalytic degradation of the contaminants in water follow the order  $\text{EE2} > \text{E2} > \text{TCS}$  as shown in Table 2. The degradation trend implies that the fast degradation observed in EE2, looking at the molecular structure of E2, EE2 and TCS in Fig. 1, the E2 contains the hydroxyl group at the C3 and C17 positions of the steroid ring structure, while the EE2 contains the ethyl group at the C17 position of the steroid structure. The TCS has two hydroxyl groups, and three chlorine atoms attached to a phenyl ring. These hydroxyl groups in E2 and the chlorinated structure in TCS make the molecule more stable and less prone to attack by reactive species, while the ethynyl group in EE2 makes it electronically unstable and prone to ROS attack. can

Additionally, the  $-\text{C}\equiv\text{CH}$  group in EE2 has a lower bond energy compared to the hydroxyl groups in E2 or the chlorinated bonds ( $\text{C}-\text{Cl}$ ) in TCS. The triple bond in EE2 is more vulnerable to attack by reactive species or the absorption of photons, which leads to the molecule breaking down [66–68].

EE2's high susceptibility to photolysis causes it to degrade more rapidly under light exposure. The  $-\text{C}\equiv\text{CH}$  group in EE2 can absorb more energy, facilitating electron transitions that result in bond breakage and the rapid formation of degradation intermediates. E2, lacking this photo-reactive  $-\text{C}\equiv\text{CH}$  group, absorbs less energy, leading to a slower rate of photolysis. TCS, with

its chlorinated structure, is even more resistant to photodegradation [16, 69].

Furthermore, the photocatalytic degradation ability of the ternary nanocomposite photocatalyst with the optimum performance of CS/KBC/GO was evaluated by carrying out the total organic carbon (TOC) analysis, the values of E2, EE2 working solution before and after the experiment was analysed to give us a clear overview into the degree of mineralization of the contaminants into  $\text{CO}_2$  and  $\text{H}_2\text{O}$ . The TOC removal (%) was observed in the range of 82.32%, 83.17% 67.37%, for E2, EE2 and TCS as shown in Fig. 9A. The mineralization trend followed  $\text{EE2} > \text{E2} > \text{TCS}$ , with TCS being the least mineralized and this reflected in the toxicity study, it has about 5% mortality on the *C. Daphnia spp* as seen in Fig. 11B.

### Influence of process variables

Different process variables such as the effect of pH, photocatalyst dose and ionic strength, effect of anions, were optimized. The influence of these variables was studied with the photocatalyst with the optimum performance for the degradation of the micropollutants (E2, EE2 and TCS), CS/KBC/GO nanocomposite photocatalyst.

Figure 8A displays how the pH affects the elimination of E2, EE2 and TCS micropollutants. The surface charge of the adsorbent is influenced by the pH which is a crucial factor in the degradation of pollutants in water. The highest degradation efficiency for E2 and EE2 was observed at a pH of 3.0, and above this pH, the efficiency reduced substantially, dropping to about 43% for E2 and 55% for EE2 in the alkaline region (pH 11.0).

CS/KBC/GO has a point of zero charge (pHpzc) of 5.31. The photocatalyst surface is positively charged below the pHpzc, and negatively charged above it. The reduction in the efficiency of CS/KBC/GO at alkaline pH could be attributed to the repulsive electrostatic interaction between the estrogen ions and graphene oxide (GO). At higher pH levels, an increase in hydroxyl ions might result in the formation of aqua complexes, which could alter or reduce the degradation efficiency of the photocatalyst [50, 51]. The pKa of E2 and EE2 are 10.71 and 10.4 respectively, making them positively charged, which explains why the efficiency increased at low pH. It suggests that hydrophobic interaction and binding affinity between E2, EE2 and selective binding sites of CS/KBC/GO were the primary driving forces for degradation.

TCS exists mainly in the protonated form when the solution pH is less than the pKa value (pKa of TCS=8.14). The deprotonated form of triclosan exists when the pH of the solution is more than 8.14, and it loses a proton making it more negatively charged. The efficiency decreases when degradation occurs at a pH

**Table 2** Kinetic parameters for the photocatalytic Degradation of E2, EE2 and TCS using CS/KBC/GO

CS/KBC/GO	$k_{app}$ ( $\text{min}^{-1}$ )	$t_{1/2}$ (min)	$r^2$
E2	0.02226	44.925	0.99392
EE2	0.03264	21.231	0.98369
TCS	0.0089	77.865	0.96754

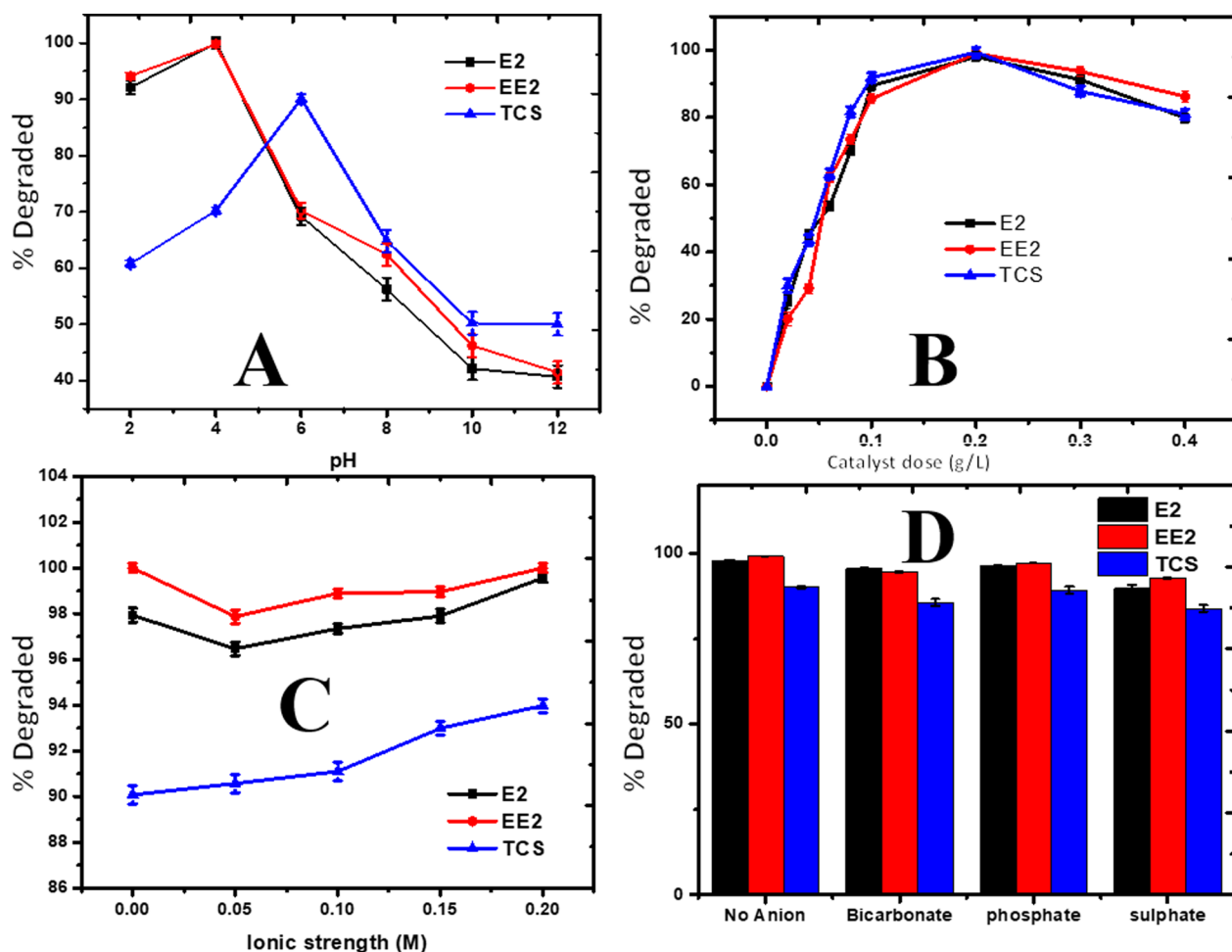


**Fig. 8** The influence of (A) Initial pH of the solution (2–12) (B) photocatalyst dose (0–0.4 g/L) (C) Ionic Strength (0–0.20 M NaCl) (D) anions (spiked with 2.0 mM of each anion) on the degradation of E2, EE2 and TCS using CS/KBC/GO. (Conditions: 100 mL of 5 mg/L EE2 and EE2, 100 mL of 10 mg/L TCS, 0.2 g CS/KBC and CS/KBC/GO, temperature 25 °C)

greater than the  $pK_a$  due to the repulsive electrostatic interaction between negatively charged ions on the photocatalyst surface and the deprotonated form of TCS. The best efficiency for TCS was observed at pH 6.0.

Figure 8B. shows that the efficiency of CS/KBC/GO for the removal of E2, EE2 and TCS increases as the photocatalyst dose increases in the mixture. The increase in efficiency as the weight increases is linked to an increase in surface area and the number of available binding sites on the surface of the photocatalyst. However, there is a decrease in photocatalyst efficiency as the dose is increased from 0.2 to 0.4 g/L. The decrease beyond the optimum dosage could be due to the overlapping of active binding sites available for degradation, which stems from overcrowding of excess photocatalyst particles.

Figure 8C illustrates the effect of ionic strength on the efficiency of CS/KBC/GO for the removal of E2, EE2, and TCS using various concentrations of NaCl. It shows that

the degradation efficiency of CS/KBC/GO is not significantly influenced by ionic strength. This could be due to the enhanced hydrophobic interactions of the micropollutant with the photocatalyst, as adding salt can increase the hydrophobic interaction due to the salting-out effect [13]. Compounds with  $\log(K_{ow})$  values greater than 4 are hydrophobic and easily degradable [52].

Figure 8D shows the effect of inorganic anions common in drinking water. A slight decrease in the degradation efficiency was observed in the presence of sulphate because it competes with the contaminants for the active binding site on the surface of the photocatalyst. This could be attributed to the reactive species scavenging reaction through hydrogen bonds and Vander Waal forces occupying the active site of the catalyst as expressed in Eqs. 3–4



Then the metal oxide ZnO exists on the surface of the ternary nanocomposite while bicarbonate and phosphate seem to not affect the degradation efficiency of the CS/KBC/GO.

### Scavenging radicals' experiment

Photodegradation of organic contaminants may be because of the reactive species generated upon illumination of light [10], this gives rise to investigating the roles each of the reactive species played in the degradation process of E2, EE2 and TCS.

Generally, three reactive species namely the hydroxyl radicals ( $\cdot\text{OH}$ ), superoxide anion radicals ( $\cdot\text{O}_2^-$ ), and positive holes ( $\text{h}^+$ ) have been established by several researchers to play a great role in the degradation of organic contaminants in water. To deduce the photodegradation mechanism, the reactive species scavenging test experiments were conducted, Scavengers such as Ammonium oxalate (AO), isopropyl alcohol (IPA), and benzoquinone (BQ), were used to trap,  $\text{h}^+$ ,  $\cdot\text{OH}$  and  $\cdot\text{O}_2^-$ , respectively [10, 70]. The results obtained for the scavenging of active species experiments are shown in Fig. 9B, it indicates that AO did not affect the degradation process, as shown by the efficiency (80.96%, 84.28%, 72.78%) for E2, EE2 and TCS respectively, while IPA (69.96%, 64.82%, 49.16%) and BQ (43.78%, 52.26%, 36.80%) inhibited the photocatalytic degradation of E2, EE2 and TCS respectively. The highest decrease in CS/KBC/GO degradation efficiency towards E2, EE2 and TCS was obtained when BQ was introduced

into the system, suggesting that the superoxide radical played the main role in the degradation process. The role of the different scavengers for the degradation of E2, EE2 and TCS are in the order of  $\text{BQ} > \text{IPA} > \text{AO}$ .

### Mechanism for the removal of the micropollutants (E2, EE2 and TCS)

The plausible removal mechanism of E2, EE2 and TCS onto the ternary nanocomposite CS/KBC/GO was achieved by adsorption and photocatalytic REDOX reactions of photocatalyst. The components which are chitosan, graphene oxide and clay, biochar (KBC) played a role in the adsorption of the micropollutant.

The octanol–water partition coefficient ( $K_{\text{now}}$ ) of E2, EE2 and TCS are 3.67–4.15, 3.94–4.01 and 4.67 respectively, which is very high making them more hydrophobic, this results in them being favourably attached to the surface of the CS/KBC/GO via  $\pi$ - $\pi$  and hydrophobic interaction as shown in the mechanism scheme in Fig. 10. The addition of GO to the binary nanocomposite CS/KBC improved the surface chemistry, which aids the removal of the micropollutants.

The photodegradation of the micropollutants E2, EE2 and TCS under visible light, may be linked to the generation of reactive species [71]. From the scavenging experiment, it was established that the superoxide and hydroxyl ion radicals were the main reactive species working towards the degradation of the micropollutants.

This test suggests the generation of positive holes  $\text{h}^+$ , and negative electrons  $\text{e}^-$  from the valence and conduction band respectively, upon the absorbance of light by the ternary nanocomposite CS/KBC/GO.

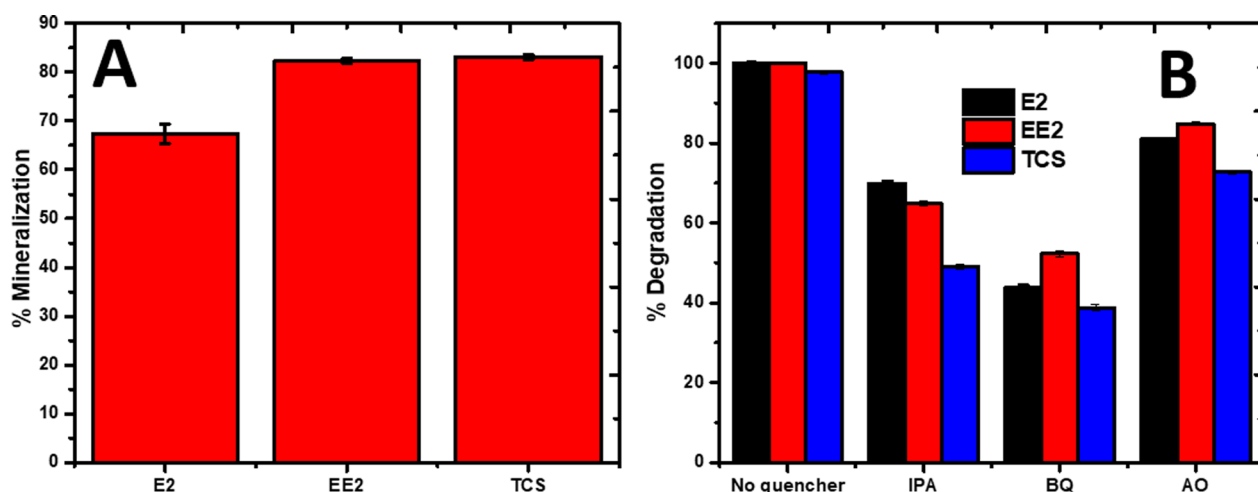


**Fig. 9** **A** % mineralization of E2, EE2 and TCS using CS/KBC/GO and **B** Effect of scavengers on the performance of CS/KBC/GO for the degradation of E2, EE2 and TCS. Conditions: 100 mL of 5 mg/L E2 and EE2, 100 mL of 10 mg/L TCS, 0.2 g CS/KBC and CS/KBC/GO, (temperature 25 °C, pH 3 for E2 and EE2 and pH 6 for TCS)

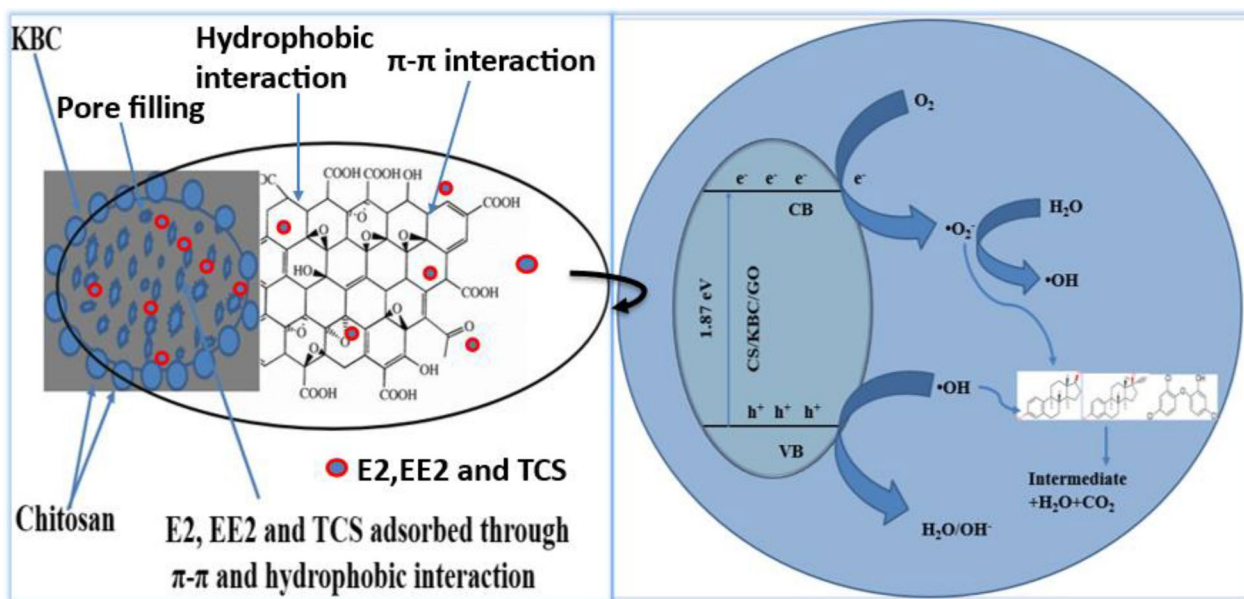
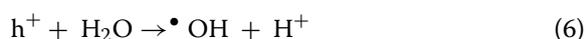
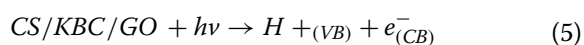


**Fig. 10** Plausible scheme showing the photodegradation mechanism for the removal of E2, EE2 and TCS using CS/KBC/GO

The photogenerated holes  $h^+$  in the valence band react with  $H_2O$  molecules to produce  $H^+$  and  $\bullet OH$  while the electron  $e^-$  in the conduction band generates  $\bullet O_2^-$  from the reduction of  $O_2$  which promotes the formation of  $H_2O_2$ , which further breaks down to  $OH^-$  and  $\bullet OH$  radicals. The  $\bullet OH$  and  $\bullet O_2^-$  radicals react with micropollutants E2, EE2 and TCS, photo-oxidizing their molecules and degrading them into less toxic molecules, with  $CO_2$  and  $H_2O$  as the end-product, Eqs. 5 to 12 describe the REDOX pathway for the mechanism.

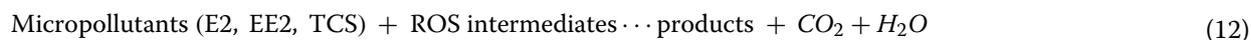


The major problem of recombination of the electron-hole pair was overcome by the presence of the KBC which is the carbon source, which acts as an electron sink [70] and GO which also serves as a carbon source and a co-catalyst, thereby trapping the  $h^+$  and  $e^-$  generated from interacting, giving room for more production of reactive species for the degradation of the micropollutants as shown in the scheme presented in Fig. 10.

This architecture maximizes charge separation and allows both electrons and holes to remain active in their respective processes, leading to higher rates of ROS generation and improved photocatalytic performance.

#### Competitive degradation of the micropollutant

The efficiency of the nanocomposite (CS/KBC/GO) in the presence of the mixture of the micro pollutant E2, EE2 and TCS at different concentrations, (E2=5 mg/L, EE2=5 mg/L, TCS=10 mg/L) was studied. Figure 11A shows the order of removal of the micropollutant is  $E2 > TCS > EE2$  with the percentage of removal being 98.25%, 82.45%, and 91.9%, respectively. This suggests the efficiency of CS/KBC/GO of the removal of EE2, E2 and TCS was good as there was only a slight drop in the degradation of E2.



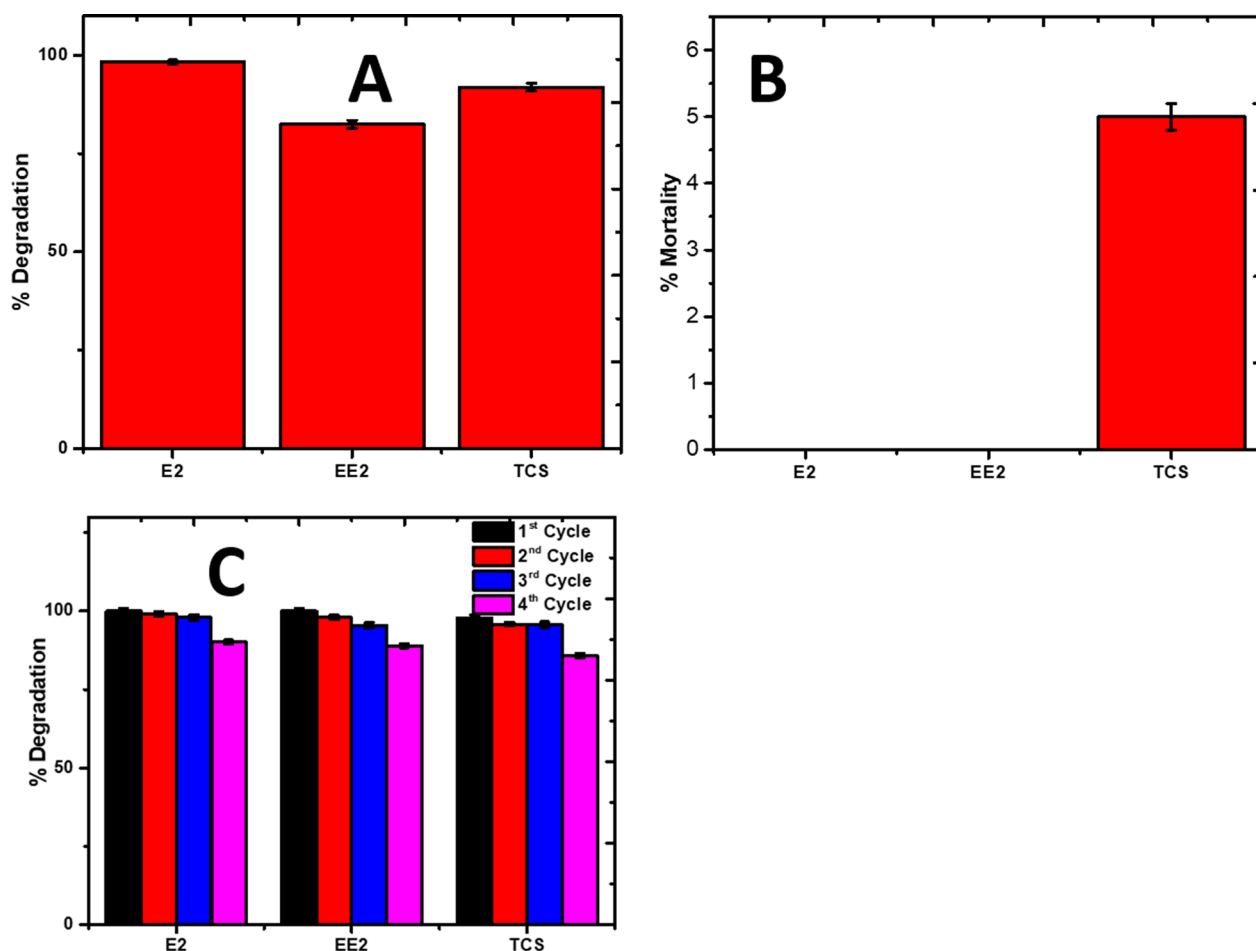


**Fig. 11** **A** competitive degradation between E2, EE2 and TCS using CS/KBC/GO, **B** % mortality of Cerio Daphnia spp. when interacted with the degraded effluent of E2, EE2 and TCS (**C**). Reuse efficiency using CS/KBC/GO for the degradation of E2, EE2 and TCS over 4 cycles. (Conditions: 100 mL of 5 mg/ LE2 and EE2, 100 mL of 10 mg/L TCS, 0.2 g CS/KBC and CS/KBC/GO, temperature 25 °C, pH 3 for E2 and EE2 and pH 6 for TCS)

### Reuse efficiency

To ascertain the stability and reuse efficiency of CS/KBC/GO a reuse efficiency test was carried out. After every trial, the photocatalyst was retrieved, washed with methanol severally, followed by Millipore water, and then dried in the oven at 60 °C for 5 h before being used again. The samples were analyzed three times. Figure 11C shows that CS/KBC/GO is stable for four cycles and does not show a significant loss of efficiency over the evaluated cycle. This result confirmed the efficiency and sustainability of the synthesized composite for the degradation of E2, EE2 and TCS in water.

The deactivation of catalysts can occur when the catalyst's active component leaches into the reaction medium, particularly in liquid-phase reactions. A leaching test was conducted, and it was found that there was no leaching of zinc into the solution. The catalyst's stability may be attributed to the strong interaction between the support

and the semiconductor. Additionally, the chitosan in the component prevents agglomeration, ensuring that they remain dispersed and active throughout multiple cycles.

Comparing the nanocomposites CS/KBC and CS/KBC/GO with other nanocomposites reported in the literature for the photodegradation of E2, EE2 and TCS from water, showed that CS/KBC and CS/KBC/GO nanocomposites were effective for the removal of these contaminants as shown in Table 3 below.

### Treatment of waste effluent and tap water.

To assess the effectiveness of CS/KBC/GO nanocomposite in eliminating micropollutants E2, EE2, and TCS from tap water and wastewater, the concentration of these substances was elevated to 5 mg/L and 10 mg/L respectively. As a control experiment, Millipore water was spiked with the same concentration of estrogens. The presence of these micropollutants in

**Table 3** Comparison of the as-synthesized photocatalysts with other photocatalysts in the literature

Photocatalyst	Contaminant	Degradation (%)	Reaction Conditions	Reuse Cycle	Reaction Time	References
Lignin Nanorod/g-C <sub>3</sub> N <sub>4</sub>	TCS	99.5	Conc:10 mg/L; pH 3	5	90	[72]
NiCu/Nb <sub>2</sub> O <sub>5</sub>	E2	82	Conc:1.5 mg/L; pH 3	–	240	[73]
Sr/Ag-TiO <sub>2</sub>	EE2	79	Conc:10 mg/L; pH -	–	240	[74]
Cds@TiO <sub>2</sub> -Rgo	E2	67.5	Conc:10 mg/L; pH -	–	120	[75]
TiO <sub>2</sub> /UV-A	TCS	82	Conc:10 mg/L; pH 7	–	20	[76]
Mixed Phase TiO <sub>2</sub> /ZnO/UV	EE2	100	Conc:10 mg/L; pH -	3	240	[77]
	E2	20		3		
BiVO <sub>4</sub>	TCS	73	Conc:10 mg/L; pH -	–	120	[78]
Ag/BiVO <sub>4</sub> /5% wt % Rgo	TCS	100	Conc:10 mg/L; pH -	3	120	[78]
Ag/AgCl/ZnFe <sub>2</sub> O <sub>4</sub>	EE2	100	Conc:5 mg/L; pH -	5	240	[79]
ZnFe <sub>2</sub> O <sub>4</sub>	EE2	30	Conc:5 mg/L; pH -	–	240	[79]
TNTs@AC	E2	99.8	Conc:5 mg/L; pH 3	–	120	[2]
Solar/TiO <sub>2</sub> -FeZ/H <sub>2</sub> O <sub>2</sub> Process	E2	78.1	Conc:5 mg/L; pH -	–	240	[80]
Aeroxide TiO <sub>2</sub> P25	E2	41.3	Conc:5 mg/L; pH -	–	240	[80]
Solar/TiO <sub>2</sub> -SnS/H <sub>2</sub> O <sub>2</sub> process	E2	51.0	Conc: 10 mg/L; pH -	–	240	[80]
Solar/ TiO <sub>2</sub> -SnS	E2	34.4	Conc: 10 mg/L; pH -	–	240	[80]
CS/KBC	E2	64.6	Conc:5 mg/L for E2	–	60	This study
	EE2	68.12	and EE2, 10 mg/L for TCS;	–	60	
	TCS	67.85	pH 3 and pH 7 for TCS	–	120	
CS/KBC/GO	E2	100	Conc:5 mg/L for E2	4	60	This study
	EE2	100	and EE2, 10 mg/L for TCS;	4	60	
	TCS	97.8	pH 3 and pH 7 for TCS	4	120	

**Table 4** Percentage removal of E2, EE2 and TCS in Millipore water, tap water and wastewater samples using CS/KBC/GO

	E2% removal	EE2% removal	TCS % removal
Millipore water	100	100	97.80
Tap water	88.13	92.34	83.25
Wastewater	83.61	84.26	79.87

the water was then measured, and the results indicated that only the wastewater sample contained a measurable concentration of estrogens before spiking, which was expected given its complex composition. According to Table 4, the levels of micropollutant removal varied in the order of Millipore water (control) > tap water > wastewater. When the nanocomposite was used with the wastewater, its effectiveness decreased, possibly due to the complexity of the sample, which caused other substances to compete for the active sites on the nanocomposite surface.

#### Toxicity test

To ascertain the toxicity effect of the treated effluent on *Ceriodaphnia spp.* The acute toxicity procedure was followed as reported in our previous study [10]. From the result, it can be deduced that TCS was the only contaminant that showed a lethal effect on the *Ceriodaphnia spp.* Population. It is safe to say the treated effluent is not toxic (Fig. 10 B).

#### Economic Evaluation and cost analysis of the as synthesized photocatalysts

The selection of a photocatalyst for the removal of E2, EE2, and TCS is crucial in achieving the sustainable development goal of providing clean water, particularly for developing countries. For this reason, this study aims to synthesize a low-cost photocatalyst while considering factors such as efficiency, cost, and energy implications. To ensure that the as-synthesized photocatalyst CS/KBC/GO is sustainable and cost-effective, it is necessary to estimate and compute the cost. This involves considering different steps in the synthesis process, from raw materials acquisition to the recovery or reuse step [50, 81]. The total cost of synthesizing CS/KBC/GO is outlined in Table 5.

Furthermore, the photocatalyst synthesis cost was calculated using the formula in Eq. 13.

**Table 5** CS/KBC/GO cost analysis

Process	Subsection	Breakdown	Cost (USD/Kg)
Material processing	Kaolinite	30 g of Kaolinite	0
	Chitosan	10 g of chitosan	74.38
	<i>Carica papaya</i> seeds	10 g of <i>Carica papaya</i> seeds	0
	Graphite	70 g of graphite	71.22
CS/KBC/GO Synthesis	ZnCl <sub>2</sub>	Cost of the ZnCl <sub>2</sub> used per g	27.8
	NaOH	Cost of the NaOH used per g	6
	H <sub>2</sub> O <sub>2</sub>	Cost of the H <sub>2</sub> O <sub>2</sub> used per g	25.8
	H <sub>2</sub> SO <sub>4</sub> /H <sub>3</sub> PO <sub>4</sub>	Cost of H <sub>2</sub> SO <sub>4</sub> /H <sub>3</sub> PO <sub>4</sub> used per g	4.2/3.8
	Drying cost	Power of oven X (kW) run time (h) X cost per hour kW.h	4
	Calcination cost	Power of microwave X (kW) run time (h) X cost per hour kW.h	3
	Sonication cost	Power of Sonicator X (kW) run time (h) X cost per hour kW.h =	2
Net cost			222.2
Overhead cost (@10% of net)			22.22
Total cost			244.42

$$\text{degradation cost} = \frac{\text{USD}}{\text{g of photocatalyst}} = \frac{\left( \text{Chemical purchase} \left[ \frac{\text{USD}}{\text{g}} \right] + \text{Energy cost} \left[ \frac{\text{USD}}{\text{g}} \right] \text{ kWh} \right)}{\text{degradation capacity efficiency}} \quad (13)$$

The total cost of synthesizing 1 kg of CS/KBC/GO is USD 244.424, which makes it an affordable and sustainable option for point-of-use/portable systems or large-scale industrial applications.

The cost of their materials is not often reported in many studies. In a recent study conducted by Akpotu et al. the reported cost for synthesizing 0.5 M-rGO-PEG was 2,811.54 USD. This material was used to remove enrofloxacin [50]. When compared to the cost of synthesis of CS/KBC/GO which is 244.42 USD, our photocatalyst is confirmed to be cheaper.

## Conclusion

CS/KBC and CS/KBC/GO nanocomposite were successfully synthesized and characterized using different techniques. The nanocomposite is composed of chitosan, biochar, Zinc oxide and graphene oxide; it is mesoporous as confirmed by the BET with a high surface area of 128 and 168 m<sup>2</sup>/g for CS/KBC and CS/KBC/GO, the increase in the surface area of CS/KBC/GO was due to the presence of GO which has been confirmed to have high surface area. The optical characterization of the nanocomposite was also evaluated, and it proved that the nanocomposite was photocatalytic and active in the visible region of the spectrum, with the degradation efficiency of the nanocomposite 100% for 5 mg/L E2,

EE2 after 60 min and 10 mg/L 97.8% after 120 min for TCS, even in the cocktail mixture the efficiency was still optimum. The degradation performance was not affected by the presence of ionic interference due to salting out effect and the presence of sulphate affected the degradation efficiency because of its ability to compete for the active sites with the contaminants. The toxicity test result showed that the treated effluent of E2 and EE2 had a slight effect on the *C. daphnia spp* while the TCS-treated effluent had a slight effect of 5% on the *C. daphnia spp*.

CS/KBC/GO proved to be a good material using the synergistic effect of both adsorption and photodegradation for the removal of E2, EE2 and TCS from water through different mechanisms such as π-π, hydrophobic interaction and by the presence of free radicals (•OH and •O<sub>2</sub><sup>-</sup>), it was possible to break bonds in the micropollutants. CS/KBC/GO was observed to be efficient even after 4 cycles of degradation of the micropollutants proving sustainable.

## Abbreviations

ZnO	Zinc oxide
GO	Graphene oxide
E2	Estradiol
EE2	17α-Ethynyl Estradiol
TCS	Triclosan
BET	Brunauer–Emmett–Teller
NMR	Nuclear Magnetic Resonance
XRD	Xray diffraction
SEM	Scanning electron microscopy
FTIR	Fourier-transformed infrared spectroscopy
UV-DRS	Ultraviolet–Visible diffuse reflectance spectroscopy

EDCs	Endocrine-disrupting chemicals
PCPs	Personal care products
CS	Chitosan
AO	Ammonium oxalate
XPS	X-ray photoelectron spectroscopy
IPA	Isopropyl alcohol
BQ	Benzoquinone
O <sub>2</sub>	Superoxide
OH	Hydroxyl
H <sup>+</sup>	Hole
K	Kaolinite
BC	Biochar

### Acknowledgements

AAB thanks the World Academy of Sciences-Brazilian National Council for Scientific and Technological Development (TWAS-CNPq) award number 315710/2018-7. EIU appreciates the equipment support from the Alexander von Humboldt Foundation for the purchase of TOC equipment used in this study. AAB appreciates Prof Helmut Eckert and his research group for their assistance with the NMR characterization of the nanocomposites.

### Author contributions

B.A.A. contributions to the conception of design of the work, acquisition, analysis, interpretation of data and funding acquisition. S.A. contributed to the analysis and writing of the original draft. O.M. supervised and revised the work. E.M.V. supervised the work and contributed to the formal analysis, and fund acquisition. E.I.U. supervised the work, substantively revised it and interpreted some data.

### Funding

The project was supported by the World Academy of Sciences-Brazilian National Council for Scientific and Technological Development (TWAS-CNPq) award number 315710/2018-7.

### Availability of data and materials

The datasets used and/or analyzed during the current study are available from the corresponding author upon reasonable request.

### Declarations

#### Ethics approval and consent to participate

Not applicable.

#### Consent for publication

Not applicable.

#### Competing interests

The authors declare no competing interests.

Received: 5 September 2024 Accepted: 29 November 2024

Published online: 18 December 2024

### References

- Diamanti-Kandarakis E, Bourguignon J-P, Giudice LC, Hauser R, Prins GS, Soto AM, Zoeller RT, Gore AC. Endocrine-disrupting chemicals: an endocrine society scientific statement. *Endocr Rev.* 2009;30(4):293–342.
- Huang T, Pan B, Ji H, Liu W. Removal of 17 $\beta$ -estradiol by activated charcoal supported titanate nanotubes (TNTs@AC) through initial adsorption and subsequent photo-degradation: intermediates DFT calculation, and mechanisms. *Water.* 2020;12(8):2121.
- Dada AO, Inyinbor AA, Tokula BE, Bayode AA, Obayomi KS, Ajanaku CO, Adekola FA, Ajanaku KO, Pal U. Zinc oxide decorated plantain peel activated carbon for adsorption of cationic malachite green dye: mechanistic, kinetics and thermodynamics modeling. *Environ Res.* 2024;252:119046. <https://doi.org/10.1016/j.envres.2024.119046>.
- G. Winkler, Occurrence and fate of triclosan and tetracycline in full-scale wastewater treatment plants, *Environmental Science Chemistry*, 2005.
- Moazeni M, Reza Maracy M, Ghazavi R, Bedia J, Andrew Lin K-Y, Ebrahimi A. Removal of triclosan from aqueous matrixes: a systematic review with detailed meta-analysis. *J Mol Liq.* 2023;376:121450. <https://doi.org/10.1016/j.molliq.2023.121450>.
- Bilal M, Barceló D, Iqbal HM. Occurrence, environmental fate, ecological issues, and redefining of endocrine disruptive estrogens in water resources. *Sci Total Environ.* 2021;800:149635.
- Tagliavini M, Nguyen MN, Schäfer AI. Predicting steroid hormone removal in a thin activated carbon layer coupled with ultrafiltration. *Chem Eng J.* 2023;462:142125.
- Bayode AA, Vieira EM, Moodley R, Akpotu S, de Camargo AS, Fatta-Kassinos D, Unuabonah EI. Tuning ZnO/GO pn heterostructure with carbon interlayer supported on clay for visible-light catalysis: removal of steroid estrogens from water. *Chem Eng J.* 2020;420:127668.
- Sornalingam K, McDonagh A, Zhou JL. Photodegradation of estrogenic endocrine disrupting steroidal hormones in aqueous systems: progress and future challenges. *Sci Total Environ.* 2016;550:209–24.
- Bayode AA, dos Santos DM, Omorogie MO, Olukanni OD, Moodley R, Bodede O, Agunbiade FO, Taubert A, de Camargo AS, Eckert H. Carbon-mediated visible-light clay-Fe<sub>2</sub>O<sub>3</sub>-graphene oxide catalytic nanocomposites for the removal of steroid estrogens from water. *J Water Process Eng.* 2021;40:101865.
- Bayode AA, Olisah C, Emmanuel SS, Adesina MO, Koko DT. Sequestration of steroidal estrogen in aqueous samples using an adsorption mechanism: a systemic scientometric review. *RSC advance.* 2023;13(33):22675–97.
- Adeel M, Song X, Wang Y, Francis D, Yang Y. Environmental impact of estrogens on human, animal and plant life: a critical review. *Environ Int.* 2017;99:107–19.
- Dhillon GS, Kaur S, Pulicharla R, Brar SK, Cledón M, Verma M, Surampalli RY. Triclosan: current status, occurrence, environmental risks and bioaccumulation potential. *Int J Environ Res Pub Health.* 2015;12(5):5657–84.
- Behera SK, Oh S-Y, Park H-S. Sorption of triclosan onto activated carbon, kaolinite and montmorillonite: effects of pH, ionic strength, and humic acid. *J Hazard Mater.* 2010;179(1–3):684–91.
- Hontela A, Habibi HR. Personal care products in the aquatic environment: a case study on the effects of triclosan in fish, fish physiology. Amsterdam: Elsevier; 2013. p. 411–37.
- Chen K, Song C, Huang Z, Rao L, Jin X, Liu G, He F, Huang Q. Thermally regenerable FeS/N-doped biochar catalyzed peroxydisulfate oxidative destruction of aqueous triclosan. *Chem Eng J.* 2023;462:142152.
- Azqhandi MHA, Foroughi M, Yazdankish E. A highly effective, recyclable, and novel host-guest nanocomposite for Triclosan removal: a comprehensive modeling and optimization-based adsorption study. *J Colloid Interface Sci.* 2019;551:195–207.
- Zang X, Chang Q, Hou M, Wang C, Wang Z. Graphene grafted magnetic microspheres for solid phase extraction of bisphenol A and triclosan from water samples followed by gas chromatography-mass spectrometric analysis. *Anal Methods.* 2015;7(20):8793–800.
- Sabalinas D, Webb SF, Hauk A, Jacob M, Eckhoff WS. Environmental fate of triclosan in the River Aire Basin UK. *Water Res.* 2003;37(13):3145–54.
- Bayode AA, Folorunso MT, Helmreich B, Omorogie MO. Biomass-tuned reduced graphene Oxide@ Zn/Cu: benign materials for the cleanup of selected nonsteroidal anti-inflammatory drugs in water. *ACS Omega.* 2023. <https://doi.org/10.1021/acsomega.2c07769>.
- Adeola AO, Abiodun BA, Adenuga DO, Nomngongo PN. Adsorptive and photocatalytic remediation of hazardous organic chemical pollutants in aqueous medium: a review. *J Contam Hydrol.* 2022;248:104019. <https://doi.org/10.1016/j.jconhyd.2022.104019>.
- Zhou M, Chen J, Yu S, Chen B, Chen C, Shen L, Li B, Lin H. The coupling of persulfate activation and membrane separation for the effective pollutant degradation and membrane fouling alleviation. *Chem Eng J.* 2023;451:139009.
- Yacouba ZA, Mendret J, Lesage G, Zaviska F, Brosillon S. Removal of organic micropollutants from domestic wastewater: the effect of ozone-based advanced oxidation process on nanofiltration. *J Water Process Eng.* 2021;39:101869.
- Bayode AA, Emmanuel SS, Sanni SO, Olalekan OA, Ore OT, Koko DT, Omorogie MO. Current status and performance evaluation of emerging advanced remediation techniques for the removal of steroidal hormones

- in water. *Environ Chem Ecotoxicol.* 2024;6:315–37. <https://doi.org/10.1016/j.enceco.2024.07.006>.
25. Hollender J, Zimmermann SG, Koepke S, Krauss M, Mc Ardell CS, Ort C, Singer H, Von Gunten U, Siegrist H. Elimination of organic micropollutants in a municipal wastewater treatment plant upgraded with a full-scale post-ozonation followed by sand filtration. *Environ Sci Technol.* 2009;43(20):7862–9.
  26. Wang H, Wang Y, Dionysiou DD. Advanced oxidation processes for removal of emerging contaminants in water. *Water.* 2023;15(3):398. <https://doi.org/10.3390/w15030398>.
  27. Lester Y, Mamane H, Avisar D. Enhanced removal of micropollutants from groundwater, using pH modification coupled with photolysis. *Water Air Soil Pollut.* 2012;223(4):1639–47.
  28. Bayode AA, Emmanuel SS, Osti A, Olorunnisola CG, Egbedina AO, Koko DT, Adedipe DT, Helmreich B, Omorogie MO. Applications of perovskite oxides for the cleanup and mechanism of action of emerging contaminants/steroid hormones in water. *J Water Process Eng.* 2024;58:104753. <https://doi.org/10.1016/j.jwpe.2023.104753>.
  29. Saffarimandoab F, Gul BY, Tasdemir RS, Ilter SE, Unal S, Tunaboylu B, Mençelolu YZ, Koyuncu IJD, Treatment W. A review on membrane fouling: membrane modification. *J Mol Liq.* 2021;216:47–70.
  30. Devendrapandi G, Liu X, Balu R, Ayyamperumal R, Arasu MV, Lavanya M, Reddy VRM, Kim WK, Karthika P. Innovative remediation strategies for persistent organic pollutants in soil and water: a comprehensive review. *Environ Res.* 2024;249:118404.
  31. Liu H, Long J, Zhang K, Li M, Zhao D, Song D, Zhang W. Agricultural biomass/waste-based materials could be a potential adsorption-type remediation contributor to environmental pollution induced by pesticides-A critical review. *Sci Total Environ.* 2024;946:174180.
  32. Ranjith R, Maruthamuthu D, Prabhavathi SP, Rajam PS. Nanotechnology, enhanced adsorption and photocatalytic removal of cationic dyes in aqueous solutions by ternary graphene oxide-TiO<sub>2</sub>-SiO<sub>2</sub> nanocomposites. *J Nanosci.* 2019;19(9):5529–45.
  33. Bayode AA, Vieira EM, Moodley R, Akpotu S, de Camargo ASS, Fatta-Kassinos D, Unuabonah EI. Tuning ZnO/GO p-n heterostructure with carbon interlayer supported on clay for visible-light catalysis: Removal of steroid estrogens from water. *Chem Eng J.* 2021;420:127668. <https://doi.org/10.1016/j.cej.2020.127668>.
  34. Alfred MO, Moodley R, Oladoja NA, Omorogie MO, Adeyemi OG, Olorunnisola D, Msagati TAM, de Jesus Motheo A, Unuabonah EI. Sunlight-active Cu/Fe@ ZnWO<sub>4</sub>-kaolinite composites for degradation of acetaminophen, ampicillin and sulfamethoxazole in water. *Ceram Int.* 2021;47(13):19220–33.
  35. Bayode AA, Moodley R, Akpotu S, de Camargo ASS, Fatta-Kassinos D, Unuabonah EI, Vieira EM. Tuning ZnO/GO p-n heterostructure with carbon interlayer supported on clay for visible-light catalysis: removal of steroid estrogens from water. *Chem Eng J.* 2021;420:127668.
  36. Yu J, Hasi Q-M, Guo Y, Song L, Yin M, Ma L, Han Z, Xiao C, Zhang Y, Chen L. Porphyrin-Based conjugated microporous polymer loaded with nanoscale zerovalent iron for the degradation of organic pollutants under visible light. *Langmuir.* 2024. <https://doi.org/10.1021/acs.langmuir.3c03507>.
  37. Rahman TU, Roy H, Shoronika AZ, Fariha A, Hasan M, Islam MS, Marwani HM, Islam A, Hasan MM, Alsukaibi AK. Sustainable toxic dye removal and degradation from wastewater using novel chitosan-modified TiO<sub>2</sub> and ZnO nanocomposites. *J Mol Liq.* 2023;388:122764.
  38. Mosaffa E, Ramsheh NA, Banerjee A, Ghafuri H. Bacterial cellulose microfilament biochar-architected chitosan/polyethyleneimine beads for enhanced tetracycline and metronidazole adsorption. *Int J Biol Macromol.* 2024;273:132953.
  39. Tang H, Zhao Y, Shan S, Yang X, Liu D, Cui F, Xing B. Theoretical insight into the adsorption of aromatic compounds on graphene oxide. *Environ Sci Nano.* 2018;5(10):2357–67.
  40. Balakrishnan A, Chinthala M, Polagani RK. 3D kaolinite/g-C<sub>3</sub>N<sub>4</sub>-alginate beads as an affordable and sustainable photocatalyst for wastewater remediation. *Carbohydr Polym.* 2024;323:121420.
  41. Murtaza G, Ahmed Z, Valipour M, Ali I, Usman M, Iqbal R, Zulfiqar U, Rizwan M, Mahmood S, Ullah A. Recent trends and economic significance of modified/functionalized biochars for remediation of environmental pollutants. *Sci Rep.* 2024;14(1):217.
  42. Thakur S, Bi A, Mahmood S, Sharma S, Ruzimuradov O, Gupta R, Cho J, Prakash J. Graphene oxide as an emerging sole adsorbent and photocatalyst: Chemistry of synthesis and tailoring properties for removal of emerging contaminants. *Chemosphere.* 2024;352:141483.
  43. Son Tran V, Hao Ngo H, Guo W, Ha Nguyen T, Mai Ly Luong T, Huan Nguyen X, Lan Anh Phan T, Trong Le V, Phuong Nguyen M, Khai Nguyen M. New chitosan-biochar composite derived from agricultural waste for removing sulfamethoxazole antibiotics in water. *Bioresour Technol.* 2023;385:129384. <https://doi.org/10.1016/j.biortech.2023.129384>.
  44. Mosaffa E, Patel D, Ramsheh NA, Patel RI, Banerjee A, Ghafuri H. Bacterial cellulose microfibril reinforced hollow chitosan beads decorated with cross-linked melamine plates for the removal of the Congo red. *Int J Biol Macromol.* 2024;254:127794.
  45. Kumar-Krishnan S, Prokhorov E, Hernández-Iturriaga M, Mota-Morales JD, Vázquez-Lepe M, Kovalenko Y, Sanchez IC, Luna-Bárceñas G. Chitosan/silver nanocomposites: synergistic antibacterial action of silver nanoparticles and silver ions. *Eur Polymer J.* 2015;67:242–51.
  46. Aouadi A, Hamada Saud D, Rebiai A, Achouri A, Benabdesselam S, Mohamed Abd El-Mordy F, Pohl P, Ahmad SF, Attia SM, Abulkhair HS, Ararem A, Messaoudi M. Introducing the antibacterial and photocatalytic degradation potentials of biosynthesized chitosan, chitosan-ZnO, and chitosan-ZnO/PVP nanoparticles. *Sci Rep.* 2024;14(1):14753. <https://doi.org/10.1038/s41598-024-65579-z>.
  47. Akpotu SO, Lawal IA, Moodley B, Ofomaja AE. Covalently linked graphene oxide/reduced graphene oxide-methoxyether polyethylene glycol functionalised silica for scavenging of estrogen: adsorption performance and mechanism. *Chemosphere.* 2020;246:125729.
  48. Unuabonah EI, Günter C, Weber J, Lubahn S, Taubert A. Hybrid clay: a new highly efficient adsorbent for water treatment. *ACS Sustain Chem Eng.* 2013;1(8):966–73.
  49. Akpotu SO, Lawal IA, Diagboya PN, Mtunzi FM, Ofomaja AE. Engineered geomedial kaolin clay-reduced graphene oxide-polymer composite for the remediation of olaquinox from water. *ACS Omega.* 2022;7(38):34054–65.
  50. Akpotu SO, Diagboya PN, Lawal IA, Sanni SO, Pholosi A, Peleyeju MG, Mtunzi FM, Ofomaja AE. Designer composite of montmorillonite-reduced graphene oxide-PEG polymer for water treatment: enrofloxacin sequestration and cost analysis. *Chem Eng J.* 2023;453:139771. <https://doi.org/10.1016/j.cej.2022.139771>.
  51. Lustriane C, Dwivany FM, Suendo V, Reza M. Effect of chitosan and chitosan-nanoparticles on post harvest quality of banana fruits. *J Plant Biotechnol.* 2018;45(1):36–44.
  52. Usman UL, Allam BK, Sajad S, Singh NB, Banerjee S. Plant leaves extract assisted eco-friendly fabrication of ZnO-SnO<sub>2</sub>/Chitosan for UV-induced enhanced photodegradation of single and ternary mixtures of Rhodamine B. *Nano-Struct Nano-Object.* 2024;37:101072. <https://doi.org/10.1016/j.nanoso.2023.101072>.
  53. Bayode AA, Vieira EM, Moodley R, Akpotu S, de Camargo AS, Fatta-Kassinos D, Unuabonah EI. Tuning ZnO/GO pn heterostructure with carbon interlayer supported on clay for visible-light catalysis: removal of steroid estrogens from water. *Chem Eng J.* 2021;420:127668.
  54. Heux L, Brugnerotto J, Desbrieres J, Versali M-F, Rinaudo M. Solid state NMR for determination of degree of acetylation of chitin and chitosan. *Biomacromol.* 2000;1(4):746–51.
  55. Mourya V, Inamdar N, Choudhari YM. Chitooligosaccharides: synthesis, characterization and applications. *Olym Sci Ser A.* 2011;53:583–612.
  56. Johra FT, Lee J-W, Jung W-G. Facile and safe graphene preparation on solution based platform. *J Ind Eng Chem.* 2014;20(5):2883–7.
  57. Stankovich S, Dikin DA, Piner RD, Kohlhaas KA, Kleinhammes A, Jia Y, Wu Y, Nguyen ST, Ruoff RS. Synthesis of graphene-based nanosheets via chemical reduction of exfoliated graphite oxide. *Carbon.* 2007;45(7):1558–65.
  58. Córdova BM, Santa Cruz JP, Huamani-Palomino RG, Baena-Moncada AM. Simultaneous adsorption of a ternary mixture of brilliant green, rhodamine B and methyl orange as artificial wastewater onto biochar from cocoa pod husk waste. Quantification of dyes using the derivative spectrophotometry method. *New J Chem.* 2020;44(20):8303–16.
  59. Houdellier F, Masseboeuf A, Monthieux M, Hytch MJ. New carbon cone nanotip for use in a highly coherent cold field emission electron microscope. *Carbon.* 2012;50(5):2037–44.

60. Idström A, Schantz S, Sundberg J, Chmelka BF, Gatenholm P, Nordstierna L.  $^{13}\text{C}$  NMR assignments of regenerated cellulose from solid-state 2D NMR spectroscopy. *Carbohydr Polym*. 2016;151:480–7.
61. Fu L, McCallum SA, Miao J, Hart C, Tudryn GJ, Zhang F, Linhardt RJ. Rapid and accurate determination of the lignin content of lignocellulosic biomass by solid-state NMR. *Fuel*. 2015;141:39–45.
62. Bayode A, Osti A, Glisenti A. Sonophotocatalytic degradation of sulfamethoxazole using lanthanum ferrite perovskite oxide anchored on an ultrasonically exfoliated porous graphitic carbon nitride nanosheet. *RSC Adv*. 2024;14(31):22063–75.
63. Nxele SR, Nyokong T. Time-dependent characterization of graphene quantum dots and graphitic carbon nitride quantum dots synthesized by hydrothermal methods. *Diam Relat Mater*. 2022;121:108751.
64. Unuabonah EI, Kolawole MO, Agunbiade FO, Omorogie MO, Koko DT, Ugwuja CG, Ugege LE, Oyejide NE, Günter C, Taubert A. Novel metal-doped bacteriostatic hybrid clay composites for point-of-use disinfection of water. *J Environ Chem Eng*. 2017;5(3):2128–41.
65. Abdullah M, Iqbal J, Rehman MSU, Khalid U, Mateen F, Arshad SN, Al-Sehemi AG, Algarni H, Al-Hartomy OA, Fazal T. Removal of ceftriaxone sodium antibiotic from pharmaceutical wastewater using an activated carbon based  $\text{TiO}_2$  composite: adsorption and photocatalytic degradation evaluation. *Chemosphere*. 2023;317:137834.
66. Yang Q, Liao W, Wei Z, Qiu R, Zheng Q, Wu Q, Chen Y. Degradation and humification of steroidal estrogens in the soil environment: a review. *Chemosphere*. 2024;357:142043.
67. Nandikes G, Pathak P, Singh L. Unveiling microbial degradation of triclosan: degradation mechanism, pathways, and catalyzing clean energy. *Chemosphere*. 2024;357:142053.
68. González-Fernández LA, Chems M, Medellín-Castillo NA, Castillo-Ramos V, Sánchez-Polo M, Vilasó-Cadre JE, Ocampo-Pérez R. Comparative kinetic analysis of triclosan degradation under UV-C and simulated solar irradiation. *Separations*. 2024;11(5):131.
69. Dong X, Yu S, Yang W, Cheng L, Tang Y, Chen D. Homogeneous oxidation of EE2 by ozone: influencing factors, degradation pathway, and toxicity assessment. *J Environ Chem Eng*. 2024;12(2):112360.
70. Bayode AA, dos Santos DM, Omorogie MO, Olukanni OD, Moodley R, Bodede O, Agunbiade FO, Taubert A, de Camargo ASS, Eckert H, Vieira EM, Unuabonah EI. Carbon-mediated visible-light clay- $\text{Fe}_2\text{O}_3$ -graphene oxide catalytic nanocomposites for the removal of steroid estrogens from water. *J Water Process Eng*. 2021;40:101865. <https://doi.org/10.1016/j.jwpe.2020.101865>.
71. Triwiswara M, Lee C-G, Moon J-K, Park S-J. Adsorption of triclosan from aqueous solution onto char derived from palm kernel shell. *Desalin Water Treat*. 2020;177:71–9.
72. Savunthari KV, Arunagiri D, Shanmugam S, Ganesan S, Arasu MV, Al-Dhahi NA, Chi NTL, Ponnusamy VK. Green synthesis of lignin nanorods/g-C $_3\text{N}_4$  nanocomposite materials for efficient photocatalytic degradation of triclosan in environmental water. *Chemosphere*. 2021;272:129801.
73. Nippes RP, Gomes AD, Macruz PD, de Souza M. Photocatalytic removal of 17 $\beta$ -estradiol from water using a novel bimetallic NiCu/Nb $2\text{O}_5$  catalyst. *Environ Sci Pollut Res*. 2023;30(47):103731–42. <https://doi.org/10.1007/s11356-023-29727-8>.
74. Wei X, Li J, Liu Z, Yang X, Naraginti S, Xu X, Wang X. Visible light photocatalytic mineralization of 17 $\alpha$ -ethinyl estradiol (EE2) and hydrogen evolution over silver and strontium modified  $\text{TiO}_2$  nanoparticles: mechanisms and phytotoxicity assessment. *RSC Adv*. 2018;8(8):4329–39.
75. Meng K, Zhou K, Chang C-T. Ultrasonic preparation of PN for the photodegradation of 17 $\beta$ -estradiol in water and biotoxicity assessment of 17 $\beta$ -estradiol after degradation. *Catalysts*. 2023;13(2):332.
76. Son H-S, Ko G, Zoh K-D. Kinetics and mechanism of photolysis and  $\text{TiO}_2$  photocatalysis of triclosan. *J Hazard Mater*. 2009;166(2–3):954–60.
77. Menon NG, George L, Tatiparti SSV, Mukherji S. Efficacy and reusability of mixed-phase  $\text{TiO}_2$ -ZnO nanocomposites for the removal of estrogenic effects of 17 $\beta$ -Estradiol and 17 $\alpha$ -Ethinylestradiol from water. *J Environ Manag*. 2021;288:112340.
78. Li M, Xu G, Guan Z, Wang Y, Yu H, Yu Y. Synthesis of Ag/BiVO $_4$ /rGO composite with enhanced photocatalytic degradation of triclosan. *Sci Total Environ*. 2019;664:230–9.
79. Upreti AR, Li Y, Khadgi N, Naraginti S, Zhang C. Efficient visible light photocatalytic degradation of 17 $\alpha$ -ethinyl estradiol by a multifunctional Ag-AgCl/ZnFe $_2\text{O}_4$  magnetic nanocomposite. *RSC Adv*. 2016;6(39):32761–9.
80. Kovacic M, Kopic N, Kusic H, Bozic AL. Solar driven degradation of 17 $\beta$ -estradiol using composite photocatalytic materials and artificial irradiation source: influence of process and water matrix parameters. *J Photochem Photobiol Chem*. 2018;361:48–61.
81. Akpotu SO, Diagboya PN, Osabohien E, Ajibola BA, Nelana SS, Mtunzi F. Beyond the boundaries of organics biosorption: reusable and cost-effective millet-straw-based carboxylate-functionalized mesoporous MCM-41. *Desalin Water Treat*. 2024;320:100805.

## Publisher's Note

Springer Nature remains neutral with regard to jurisdictional claims in published maps and institutional affiliations.